nature communications

Article

https://doi.org/10.1038/s41467-024-55263-1

Colon-targeted engineered postbiotics nanoparticles alleviate osteoporosis through the gut-bone axis

Received: 23 April 2024

Accepted: 6 December 2024

Published online: 30 December 2024

Check for updates

Tingting Yu[1,2,3,6], Rushui Bai[1,2,3,4,6], Zeming Wang[4,5,6], Yuting Qin[4,6], Jingwei Wang[1,2,3,4], Yaohua Wei[4], Ruifang Zhao[4,5] ✉, Guangjun Nie[4,5] ✉ & Bing Han[1,2,3] ✉

The potential for mitigating intestinal inflammation through the gut-bone axis in the treatment of osteoporosis is significant. While various gut-derived postbiotics or bacterial metabolites have been created as dietary supplements to prevent or reverse bone loss, their efficacy and safety still need improvement. Herein, a colon-targeted drug delivery system is developed using surface engineering of polyvinyl butyrate nanoparticles by shellac resin to achieve sustained release of postbiotics butyric acid at the colorectal site. These engineered postbiotics nanoparticles can effectively suppress macrophage inflammatory activation, modulate the redox balance, and regulate the composition of the gut microbiota, thereby restoring epithelial barriers, inhibiting bacterial invasion, and down-regulating pro-inflammatory responses. As a result, the remission of systemic inflammation is accompanied by a rebalancing of osteoblast and osteoclast activity, alleviating inflammatory bowel disease-related and post-menopausal bone loss. Specifically, the treatment of engineered postbiotics nanoparticles can also improve the quality and quantity of bone with restoration of deteriorative mechanical properties, which indicating a therapeutic potential on fracture prevention. This study provides valuable insights into the gut-bone axis and establishes a promising and safe therapeutic strategy for osteoporosis.

Osteoporosis (OP) is a chronic degenerative condition characterized by low bone mass and microarchitectural deterioration of bone tissue, with a consequent increase in bone fragility and susceptibility to fracture[1,2]. OP-related fractures, which can lead to disability and mortality, are recognized as a significant worldwide social and economic burden. Various agents have been developed to treat OP, including bisphosphonates, denosumab, selective estrogen receptor modulators, and calcitonin[3]. However, the different etiologies of OP, such as age-related bone loss, prolonged corticosteroid usage, or illnesses, challenge the efficacy of therapeutic agents. Current pharmacological treatments for osteoporosis, including bisphosphonates, antibodies, and parathyroid hormone (PTH)-related peptides, and teriparatide, exhibit limitations in their therapeutic efficacy and are associated with significant adverse effects. For example, long-term use of bisphosphonates is linked to serious complications such as osteonecrosis of the jaw and atypical femoral fractures, in addition to gastrointestinal

[1]Department of Orthodontics, Peking University School and Hospital of Stomatology, Beijing, China. [2]National Center for Stomatology, Beijing, China. [3]National Engineering Research Center of Oral Biomaterials and Digital Medical Devices, Beijing, China. [4]CAS Key Laboratory for Biomedical Effects of Nanomaterials and Nanosafety, CAS Center of Excellence in Nanoscience, National Center for Nanoscience and Technology, Beijing, China. [5]Center of Materials Science and Optoelectronics Engineering, University of Chinese Academy of Sciences, Beijing, China. [6]These authors contributed equally: Tingting Yu, Rushui Bai, Zeming Wang, Yuting Qin. ✉e-mail: zhaorf@nanoctr.cn; niegj@nanoctr.cn; kqbinghan@bjmu.edu.cn

side effects[4,5]. Similarly, denosumab has been implicated in rare instances of jaw osteonecrosis, and its discontinuation can precipitate a rebound increase in bone turnover, thereby elevating the risk of fractures[6,7]. Romosozumab, although approved, is accompanied by a black-boxed warning due to the associated risks of myocardial infarction, cerebrovascular accident, and cardiovascular mortality[8]. Moreover, teriparatide, a potent anabolic agent derived from PTH, is associated with several limitations, including restricted exposure of its active site, the requirement for intermittent systemic administration, and the potential risks of hypercalcemia and the development of osteosarcoma[9]. Thus, there is an urgent need to develop comprehensive therapeutic strategies associated with a favorable safety profile.

Recent research highlights the importance of the gut, specifically the gut microbiota and their metabolites, in regulating bone homeostasis through the "gut-bone axis"[10]. Different gastrointestinal disorders, including inflammatory bowel disease (IBD), can negatively impact bone health by impairing nutrient and calcium absorption and releasing inflammatory factors that interfere with bone resorption and formation[11,12]. In fact, OP has been considered as a co-morbidity in patients suffering from IBD, who typically present with increased fracture risk[12,13]. Thus, the maintenance of gastrointestinal homeostasis holds promise for the treatment of OP. Postbiotics, derived from commensal bacteria and include inactivated cells and cell-free supernatants, provide various health benefits to the host[14]. Utilizing postbiotics such as butyrate aims to enhance systemic bone mass by preserving gastrointestinal health through their anti-inflammatory and antioxidant properties[15–18]. However, challenges exist in controlling butyrate concentrations to avoid unintended consequences on intestinal epithelial cells and the gut barrier[19,20].

In this study, we have synthesized a shellac-engineered postbiotics nanoparticle, which exhibits targeted delivery capacity to the colon and sustained release of butyric acid. The shellac-engineered postbiotics nanoparticle effectively suppresses macrophage activation, scavenges reactive oxygen species (ROS), and restores gut microbiota balance in inflamed colon tissues. Consequently, systemic inflammation is reduced, osteoblast and osteoclast activity are rebalanced, and bone loss is mitigated in age-related primary OP and disease-induced secondary OP models (Fig. 1).

Results

Synthesis and characterization of engineered postbiotics nanoparticles

Shellac, a natural resin that exhibits a tight arrangement under acidic conditions due to carboxyl groups, was selected for the oral delivery system because of its bio-safety, colonic pH responsiveness,

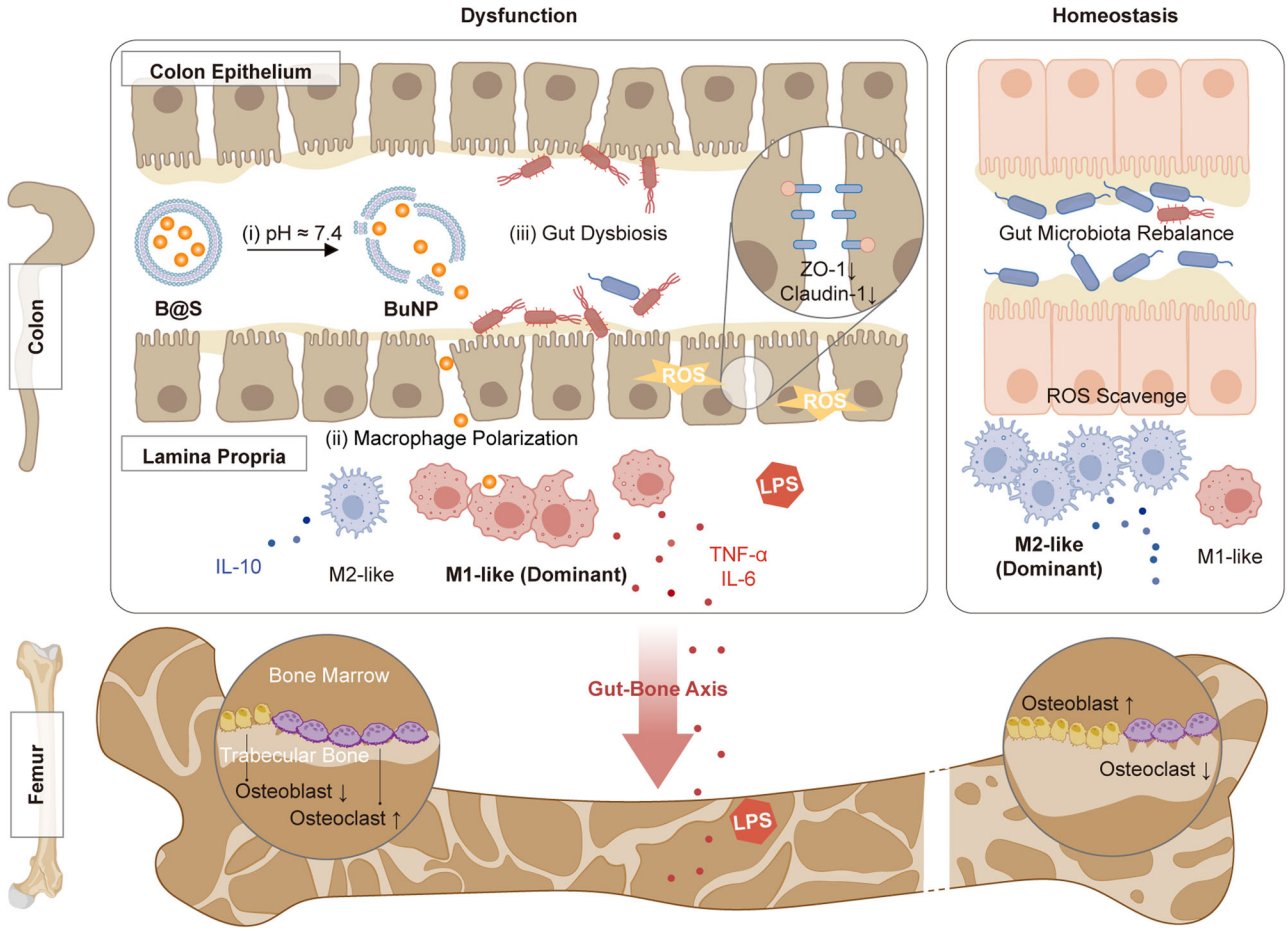

Fig. 1 | Schematic of engineered postbiotics nanoparticles in the regulation of gut-bone axis. The shellac shell protected the polyvinyl butyrate nanoparticles (BuNP), preventing degradation by gastric acid and facilitating the release of the BuNP in the lower region of the gastric intestinal tract at pH 7.4 (i). The nano-sized BuNP can then be internalized and hydrolyzed by macrophages, promoting anti-inflammatory polarity (ii). The sustained release of BuNP aids in rebalancing redox levels and gut microbiota in inflamed colon tissue (iii). Collectively, these mechanisms contribute to the efficacy of shellac-engineered postbiotics nanoparticles (B@S) in treating gut-derived inflammation and post-menopausal-induced systemic bone issues. ZO-1, zonula occludens-1. ROS, reactive oxygen species. M1-like, inflammatory phenotype of macrophages. M2-like, anti-inflammatory phenotype of macrophages. IL-10, interleukin 10. TNF-α, tumor necrosis factor-alpha. IL-6, interleukin 6. LPS, lipopolysaccharide. Created in BioRender. https://BioRender.com/n22p561.

https://doi.org/10.1038/s41467-024-55263-1

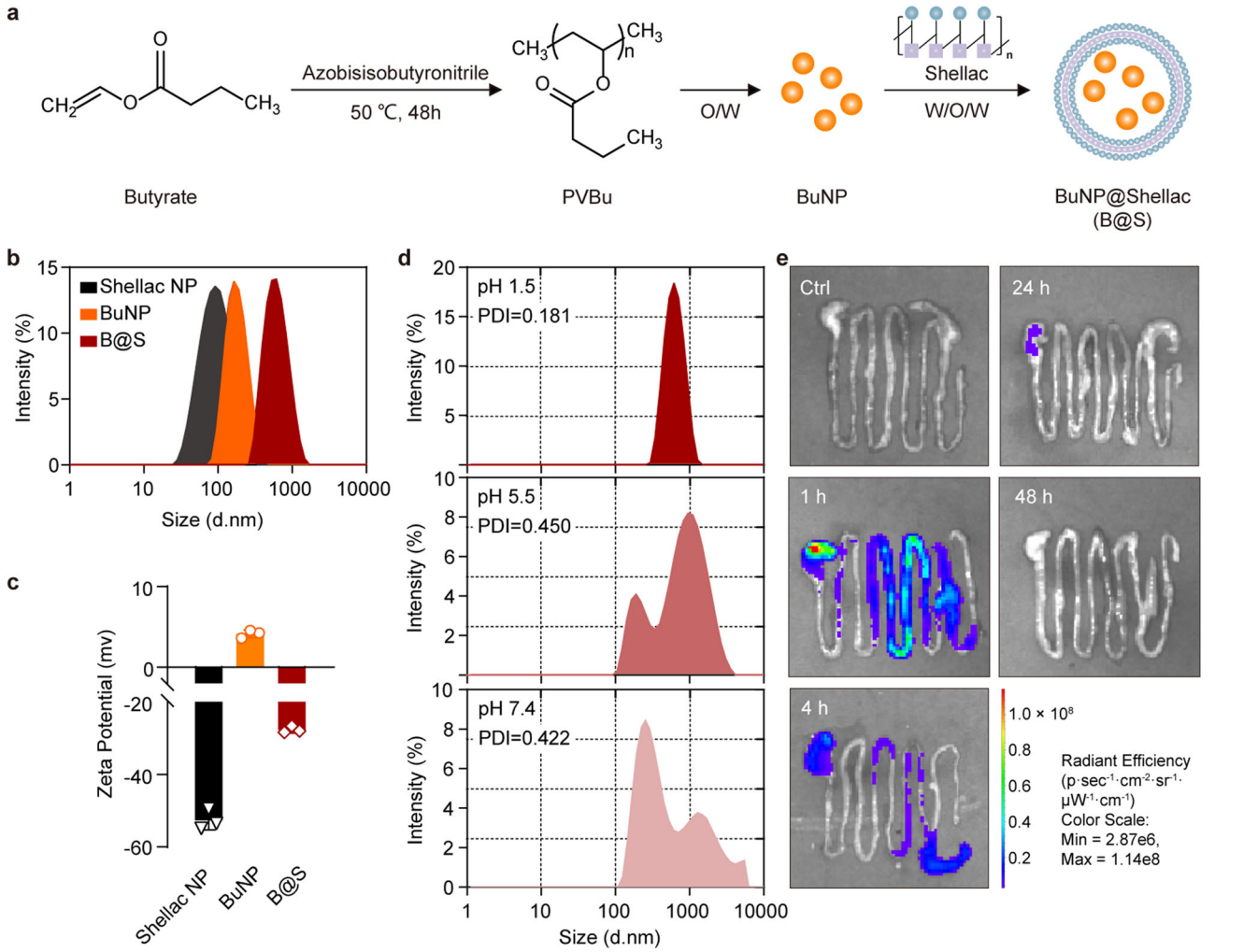

Fig. 2 | Synthesis and characterization of engineered postbiotics nanoparticles (BuNP@Shellac). a Schematic illustration of the synthetic route of B@S. Polyvinyl butyrate (PVBu) was produced by radical polymerization and then made into polyvinyl butyrate nanoparticle (BuNP). BuNP was loaded in the prepared shellac hydrogel to get BuNP@Shellac (B@S). O/W, oil-in-water. W/O/W, water-in-oil-in-water. **b**, **c** Size (**b**) and zeta potential (**c**, $n = 3$ biologically independent samples) from DLS of BuNP, shellac nanoparticles (NP), and B@S. **d** pH stability of B@S under pH 1.5, pH 5.5, and pH 7.4 during 4 h. PDI, polydisperse index. **e** In vivo fluorescence analysis of the gastrointestinal tract of C57BL/6 N mice after oral administration of fluorescence-labeled-B@S for 0 (Ctrl), 1, 4, 24 and 48 h. The Ctrl mice were administered phosphate-buffered saline (PBS). The numerical data in (**c**) are presented as mean ± standard deviation (s.d.). These experiments (**b**, **d**, **e**) were repeated three times independently with similar results. Source data are provided as a Source Data file.

amphiphilicity, and film-forming properties[21]. The butyrate-releasing composite nanoparticles BuNP@Shellac (B@S) contained polyvinyl butyrate nanoparticles (BuNP) as the core and shellac as the shell. The shellac-based coating enables the BuNP core to withstand gastric acid's corrosive effects of gastric acid and release the butyrate acid in the colon. Briefly, BuNP was produced by radical polymerization and oil-in-water emulsion solvent evaporation process. Shellac was wrapped around BuNP using a modified double-emulsion (water-in-oil-in-water) solvent evaporation/diffusion technique (Fig. 2a). Dynamic light scattering (DLS) exhibited that the diameter of B@S is more significant than the BuNP, indicating the wrapping of BuNP by shellac (Fig. 2b). Meanwhile, the surface engineering of shellac on BuNP shifted it from positive zeta potential to the negative potential of B@S, further proving the success synthesized B@S (Fig. 2c). We got spherical B@S particles revealed by scanning electron microscopy (SEM) (Supplementary Fig. 1a). B@S exhibited a clear pH-dependent destabilization, being less stable at higher pH levels (Fig. 2d). Shellac could prevent the BuNP from leaking out in the gastric acid environment (pH 1.5) since we observed that B@S maintained stability. When the pH approaches the colonic environment (pH 7.4), B@S showed a reduction in size similar to that of BuNP, indicating the dissolution of shellac led to a releasing BuNP. It is noteworthy that at elevated pH levels (pH 7.4), which are characteristic of the colonic environment, shellac dissolves, facilitating butyric acid release under these conditions (Supplementary Fig. 1b). During the first 4 h, release rates are fast, then start to decrease; after 24 h, the amount of drug released was ~60%. These findings suggest that the B@S delivery system effectively protects BuNP from the acidic gastric environment, thus enhancing targeted delivery to the colon.

To observe the biodistribution and retention of B@S in gastrointestinal (GI) tracts, 6-to-8-week-old C57BL/6 N female mice were orally gavaged fluorescence-labeled B@S. The Intelligent Visual Inspection System (IVIS) was used to visualize the spatiotemporal distribution of B@S in GI tracts. As shown in Fig. 2e, B@S reached the cecum within 1 h and accumulated in 4 h, a small amount of B@S can still be observed in 24 h and was cleared from the intestine within 48 h. We further detected the fluorescence in major organs and bone tissues, including the heart, liver, spleen, lung, kidney, and femurs. The fluorescent signals were below the detection limit in both the major organs and bone tissue, indicating negligible systemic absorption of

https://doi.org/10.1038/s41467-024-55263-1

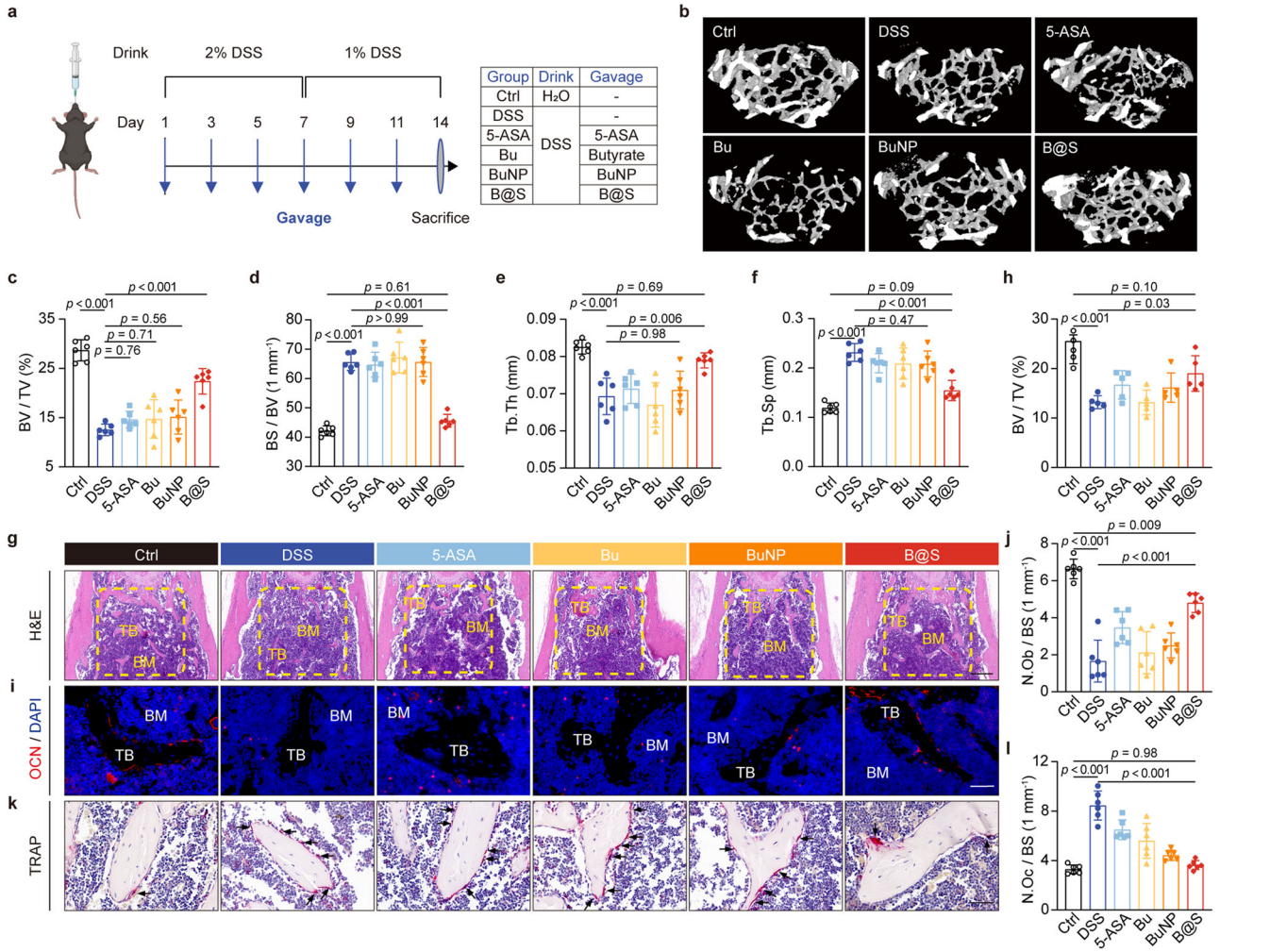

Fig. 3 | Restoration of bone mass in colitis-induced osteoporosis through osteoblast-osteoclast rebalancing. a Schematic illustration of colitis-complicated-osteoporosis therapeutic study. C57BL/6 N mice were administered 2% (w/v) DSS during the 1st week and changed with 1% (w/v) DSS during the 2nd week, along with treatments of 5-ASA, Bu, BuNP and B@S every other day for 6 times. Femurs of mice were collected after sacrifice. Created in BioRender. https://BioRender.com/w77p777. **b**–**f** Representative 3D restoration images (**b**) and quantification of BV/TV (**c**, $n = 6$ mice), BS/BV (**d**, $n = 6$ mice), Tb.Th (**e**, $n = 6$ mice) and Tb.Sp (**f**, $n = 6$ mice) of distal femurs, as scanned by μCT. **g**, **h** Representative images (scale bar, 300 μm) (**g**) and statistical quantification of trabecular area (**h**, $n = 5$ mice) of H&E staining of femurs. TB, trabecular bone. BM, bone marrow. The yellow dashed boxes on (**g**) showed the quantified area of (**h**). **i**, **j** Representative IF staining images (scale bar, 50 μm) of OCN (red) and DAPI (blue) (**i**) and analysis of OCN-positive osteoblast number/bone surface ratios (N.Ob/BS) (**j**, $n = 6$ mice). DAPI, 4′,6-diamidino-2-phenylindole. **k**, **l** Representative TRAP staining images (scale bar, 50 μm) (**k**) and analysis of osteoclast number/bone surface ratios (N.Oc/BS) (**l**, $n = 6$ mice). Black arrows on (**k**) pointed to TARP-positive osteoclasts. The numerical data in (**c**–**f**, **h**, **j**, **l**) are presented as mean ± s.d. A one-way ANOVA with Tukey's post-test for multiple comparisons (**c**–**f**, **h**, **j**, **l**) was made for statistical significance analysis. These experiments (**b**, **g**, **i**, **k**) were repeated three times independently with similar results. Source data are provided as a Source Data file.

B@S (Supplementary Fig. 1c, d). Next, to further confirm the effect of B@S on the skeletal and intestinal system in normal mice, we harvested the femurs and colon tissue of B@S-treated wild-type (WT, C57BL/6 N) mice for analysis. As shown in Supplementary Fig. 2 and Supplementary Fig. 3, B@S supplement is not able to alter the intestinal and skeletal status in WT mice. These data indicate that B@S nanoparticles can accumulate in the intestine and release butyric acid in the colon while minimizing the potential for systemic distribution-related side effects.

Engineered postbiotics nanoparticles restored osteoblast-osteoclast balance to prevent colitis-complicated osteoporosis

To explore the therapeutic potential of B@S by affecting the gut-bone axis in OP, a dextran sulfate sodium salt (DSS)-induced colitis mouse model characterized by bone loss was established[22]. The experiment procedure is shown in Fig. 3a. Consistent with previous reports[23], the epithelial tight junctions of the intestinal barrier of DSS-induced mice showed significantly decreased by assessing the levels of claudin-1 and zonula occludens-1 (ZO-1), makers of tight junctions (Supplementary Fig. 4). To further confirm the phenotype appears on skeletal system, we next investigated the bone volume through micro-computed tomography (μCT) analysis, revealing a significant decrease in bone mass in DSS-induced mice compared to the Ctrl group (Fig. 3b), as indicated by parameters such as bone volume/tissue volume (BV/TV) (Fig. 3c), bone surface/volume ratio (BS/BV) (Fig. 3d), trabecular thickness (Tb.Th) (Fig. 3e), and trabecular separation (Tb.Sp) (Fig. 3f). Accompanied by confirming that DSS, a classic inducer of colitis, can cause bone loss in mice, we also orally administered postbiotics in various forms, including free butyrate (Bu), BuNP, and B@S. In particular, 5-aminosalicylic acid (5-ASA), the first-line agent for relieving colitis, was used to investigate its ability to treat OP. Interestingly, B@S effectively rescued the bone mass, while 5-ASA, Bu, or BuNP treatment could not ameliorate colitis-associated OP. Moreover, the distal femoral trabecular bone volume was also detected by the hematoxylin-

eosin (H&E) staining; the ratio of trabecular bone toward bone tissue volume showed the same trends as μCT (Fig. 3g, h).

Bone homeostasis can be influenced by the dynamic balance between osteoblasts and osteoclasts activities. To explore if the B@S treatment could restore the bone resorption and formation rate, the histomorphometric analysis was carried out to detect the osteoblast and osteoclast activities of the femurs using osteocalcin (OCN) and tartrate-resistant acid phosphatase (TRAP) staining, respectively. The OCN-positive cells were decreased, and the TRAP-positive cells were elevated significantly in the distal femur of DSS-induced mice, as shown in the immunofluorescent (IF) staining (Fig. 3i, j) and the immunohistochemical (IH) staining (Fig. 3k, l). The B@S-treated group significantly restored OCN-positive cells and decreased TRAP-positive cells in the femurs of DSS-induced mice. In addition, serum levels of bone formation markers, OCN, and procollagen type 1 N-terminal propeptide (P1NP) were reduced, while bone resorption maker, type I collagen cross-linked telopeptide (CTX-I) was elevated in DSS-induced mice (Supplementary Fig. 5a–c). B@S treatment helped restore bone turnover makers' serum levels, including OCN, P1NP, and CTX-I, to the normal range (Supplementary Fig. 5a–c). These results suggest that overactivation of osteoclast and insufficient osteoblast function might contribute to the osteoporosis phenotype of DSS-induced mice[22]. To further confirm this observation, the calcein-labeling assay showed that bone turnover rate was decreased in DSS-induced mice, whereas B@S significantly improved bone formation and mineralization (Supplementary Fig. 5d–g). The DSS-induced reduction of maximum load and flexural strength of the femurs can also be reversed after B@S treatment (Supplementary Fig. 5h, i). Meanwhile, B@S shows excellent biosafety detected with H&E staining of major organs, including the heart, liver, spleen, lung, and kidney (Supplementary Fig. 6).

These results confirmed that colitis was not only localized but also had systemic implications such as bone disorders. B@S, a colon-accumulated postbiotics nanoparticle, could exert a protective effect on the distal organ bone, which indicated the existence of a gut-bone axis. Although the promotion of bone mass might be correlated with the re-balance between osteoblasts and osteoclasts' activities, the role of B@S in the ameliorating OP has to be first investigated in combination with its ameliorating colitis contributions.

Engineered postbiotics nanoparticle treatment effectively alleviated DSS-induced acute colitis with a remodeled gut microbiome and reduced systemic inflammation

We used the DSS-induced acute inflammatory colitis mouse model to investigate the potential of engineered postbiotics nanoparticles in alleviating intestinal inflammation. The animal experimental procedure is shown in Fig. 4a. Consistent with previous studies[24], DSS-induced colitis mice showed significant weight loss and high disease activity index (DAI). B@S treatment was able to alleviate the reduced body weight (Fig. 4b), decrease the DAI scores (Fig. 4c), and restore the colon length significantly (Fig. 4d, e). Notably, the therapeutic efficacy of B@S was even better when compared with the 5-ASA group. Moreover, Bu and BuNP failed to protect mice with colitis from body weight loss and disease development. Next, the therapeutic efficacy of engineered postbiotics nanoparticles on colitis was further verified on a histological level. As shown in Fig. 4f and Supplementary Fig. 7a, epithelial damage (loss of goblet cells and crypts) and inflammatory cell infiltration were observed in the colon tissue of DSS-induced colitis mice, which could be analyzed as histological activity index (HAI). According to HAI, B@S treatment ameliorated epithelial damage and inflammatory cell infiltration of colitis better than the Bu group ($p < 0.001$), the BuNP group ($p < 0.001$), and the 5-ASA group (no significant difference).

The epithelial tight junctions are the primary determinants of intestinal barrier function, limiting direct interactions between gut luminal contents and the underlying immune system[25]. In this case, we investigated the epithelial tight junctions of the intestinal barrier by assessing the levels of claudin-1 and ZO-1 (Fig. 4g and Supplementary Fig. 7b, c). Immunofluorescence staining revealed that the colon tissue of B@S-treated mice showed the most enriched claudin-1 and ZO-1, representing favorable epithelial barrier function, among all the other treatment groups, including Bu, BuNP, and 5-ASA groups.

Gut microbial dysbiosis, i.e., reducing microbial diversity and imbalance of beneficial and pathogenic microbes, are the critical characteristics of IBDs[26]. We performed 16S ribosomal RNA (16S rRNA) sequencing to compare the changes in gut microbiota in mice following DSS usage and treatments with different formulations. Observed operational taxonomic unit (OTU) count (Supplementary Fig. 8a) and alpha-diversity analysis of OTU level (Fig. 4h, i and Supplementary Fig. 8b, c) of the same valid reads suggested significant loss of bacterial richness in the DSS group and rescue of that in B@S-treated group. In addition, B@S treatment showed a distinct gut microbiome profile compared to DSS, 5-ASA-, Bu-, and BuNP-treated DSS group (Supplementary Fig. 8d–f). The profile of the B@S-treated group was closer to that of the Ctrl group (Fig. 4j). Specifically, B@S treatment alleviated gut microbiota dysbiosis in the DSS group and other treatment groups, appearing as increased harmful bacteria like *Escherichia-Shigella* and decreased beneficial bacteria like *Alistipes* (Fig. 4j). We also evaluated the bacterial metabolites-short chain fatty acids (SCFA) concentration of cecum feces and serum in mice *via* targeting metabolomics analysis. B@S treatment had no significant impact on the concentration of acetic acid (Supplementary Fig. 8g) and propanoic acid (Supplementary Fig. 8h) compared to the DSS group. Interestingly, we found that the DSS-induced mice exhibited an unstable distribution of endogenous butanoic acids, after treatment of B@S the distribution became even and the levels of butanoic acids elevated slightly, indicating the supplement of B@S helped maintain intestinal homeostasis (Fig. 4k). In addition, the concentration of butyrate in serum level was not changed after B@S treatment (Fig. 4l), indicating the indirect effect of butyrate through gut-bone axis instead of direct influence to the bone.

The damaged epithelial barrier in inflamed colon tissue results in molecule leakage to the circulatory system, including lipopolysaccharide (LPS) from Gram-negative bacteria and lipoteichoic acids (LTA) from Gram-positive bacteria[27–29]. As a major Gram-positive bacteria cell wall component, LTA is related to various inflammatory diseases[30]. With the increased level of LPS in the circulation, systemic inflammation can be activated, which will induce bone loss[31]. Herein, to investigate the underlying correlation between GI and skeletal system after B@S treatment, we verified serum LPS and LTA concentration by enzyme-linked immunosorbent assay (ELISA). As Fig. 4m, n showed, the concentration of LPS and LTA in DSS-induced colitis mice decreased significantly after B@S treatment. Moreover, the pro-inflammatory cytokines tumor necrosis factor-alpha (TNF-α) (Fig. 4o) and interleukin 6 (IL-6) (Fig. 4p) showed a decreased trend. In contrast, the anti-inflammatory cytokine interleukin 10 (IL-10) (Fig. 4q) could be increased significantly when detected in the mice serum after B@S treatment.

These results suggested that shellac-engineered postbiotics nanoparticles are effective for treating DSS-induced acute colitis. The core-shell structure was necessary to improve the therapeutic efficacy of butyrate and mono-butyrate nanoparticles (BuNP). B@S restored the colonic epithelial barrier integrity, preventing gut microbiota from encroaching. It also remodeled the gut microbiome to restore balance, which, taken together, reduced dysbiosis-induced systemic inflammation, as shown in Fig. 4r.

Regulation of redox balance and macrophage polarization by engineered postbiotics nanoparticles helped to protect the colonic barrier

Having confirmed the therapeutic effects on colitis and osteoporosis phenotypes, we studied the underlying mechanisms of how B@S

https://doi.org/10.1038/s41467-024-55263-1

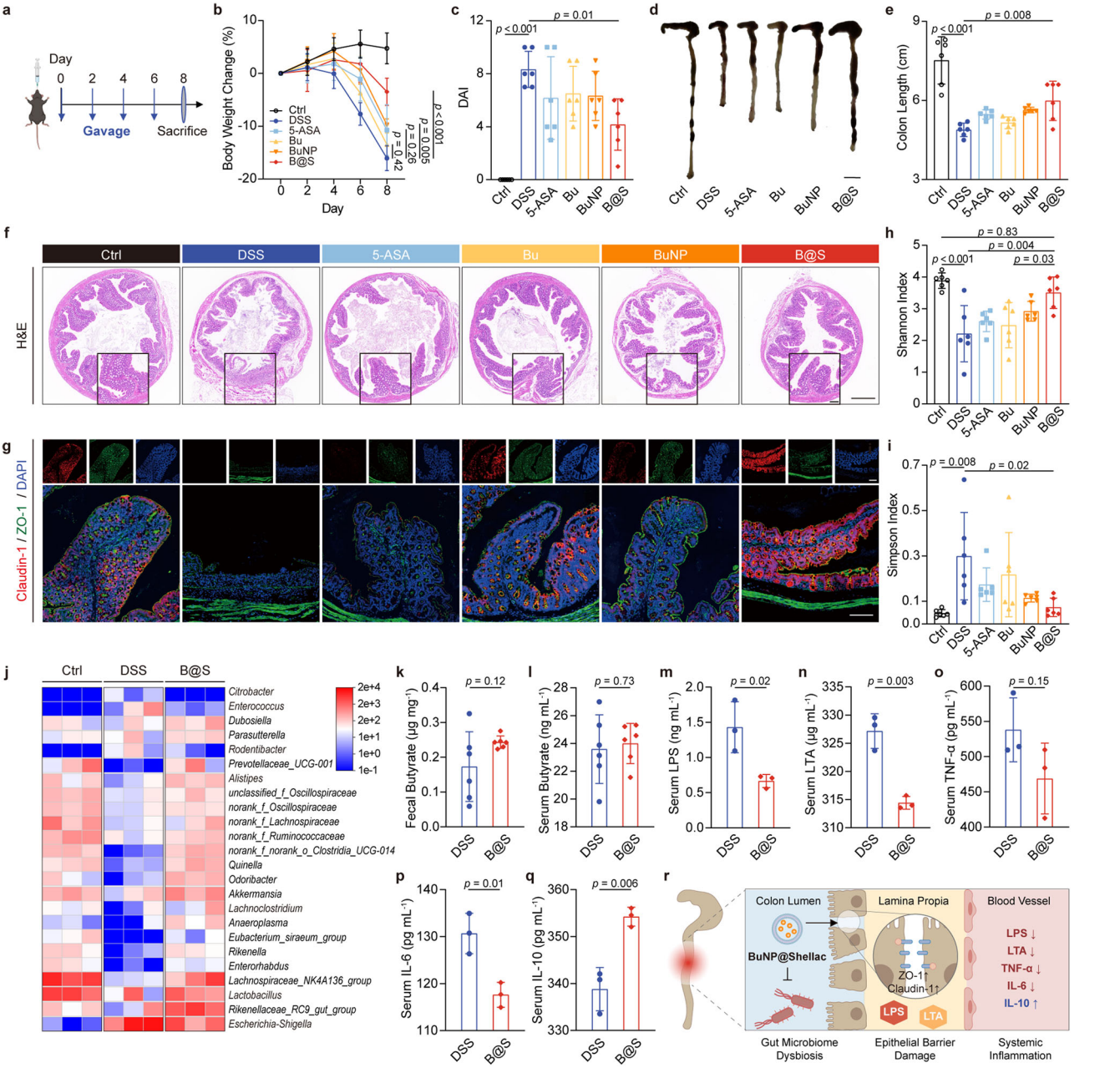

Fig. 4 | Engineered postbiotics nanoparticles alleviated DSS-induced acute colitis with remodeled gut microbiome and reduced systemic inflammation. **a** Schematic illustration of murine colitis therapeutic study. Created in BioRender. https://BioRender.com/w77p777. **b** Body weight change compared with the initial weight on day 0 during the study ($n = 6$ mice). **c** DAI of mice, representing the severity of colitis ($n = 6$ mice). **d**, **e** Representative images (**d**) and statistical length analysis (**e**, $n = 6$ mice) of colons were collected on day 8. Scale bar, 1 cm. (**f**, **g**) Representative H&E staining images (scale bars, 500 μm, and 125 μm for enlarged images) (**f**), as well as IF staining images (scale bars, 125 μm) of claudin-1 (red), ZO-1 (green) and DAPI (blue) (**g**) of colon sections. DAPI, 4′,6-diamidino-2-phenylindole. **h**–**j** Gut microbiome analysis from 16S rRNA sequencing data. Microbial community alpha-diversity was estimated through the Shannon index (**h**, $n = 6$ mice) and Simpson index (**i**, $n = 6$ mice) of the OTU level. Analysis of microbial composition was shown as a heatmap of the relative abundance at the genus level (rows) of gut microbiota after the indicated treatments (columns) (**j**, $n = 3$ mice). **k**, **l** The amount of butyrate in the feces of the cecum (**k**, $n = 6$ mice) and serum (**l**, $n = 6$ mice). (**m**–**q**) The concentration of LPS (**m**, $n = 3$ mice), LTA (**n**, $n = 3$ mice), TNF-α (**o**, $n = 3$ mice), IL-6 (**p**, $n = 3$ mice) and IL-10 (**q**, $n = 3$ mice) in serum of DSS and B@S group measured via ELISA. **r** Schematic illustration of gut microbiome dysbiosis and colonic epithelial barrier damage resulting in systemic inflammation. Created in BioRender. https://BioRender.com/x06g309. The numerical data in (**b**, **c**, **e**, **h**, **i**, **k**–**q**) are presented as mean ± s.d. A two-way ANOVA with the Geisser-Greenhouse correction (**b**), one-way ANOVA with Tukey's post-test for multiple comparisons (**c**, **e**, **h**, **i**) or two-sided unpaired Student's *t* test (**k**–**q**) was made for statistical significance analysis. These experiments (**d**, **f**, **g**) were repeated three times independently with similar results. Source data are provided as a Source Data file.

regulates local and systemic responses. We first detected the biocompatibility of BuNP by using Cell Counting Kit-8 (CCK-8) analysis to test the time-dependent cytotoxicity of Bu and BuNP toward Caco2 cells. Caco2 cells were exposed to Bu or BuNP during 1, 3, 5, and 7 d (Supplementary Fig. 9a). The result showed that Bu had apparent cytotoxicity to Caco2 cells. At the same time, BuNP exhibited good biocompatibility, having living cells similar to the phosphate-buffered saline (PBS) group's. BuNP performed better biocompatibility during 7 days, which may contribute to the steady low-concentration release of butyrate from BuNP, while high dose butyrate could affect cell

https://doi.org/10.1038/s41467-024-55263-1

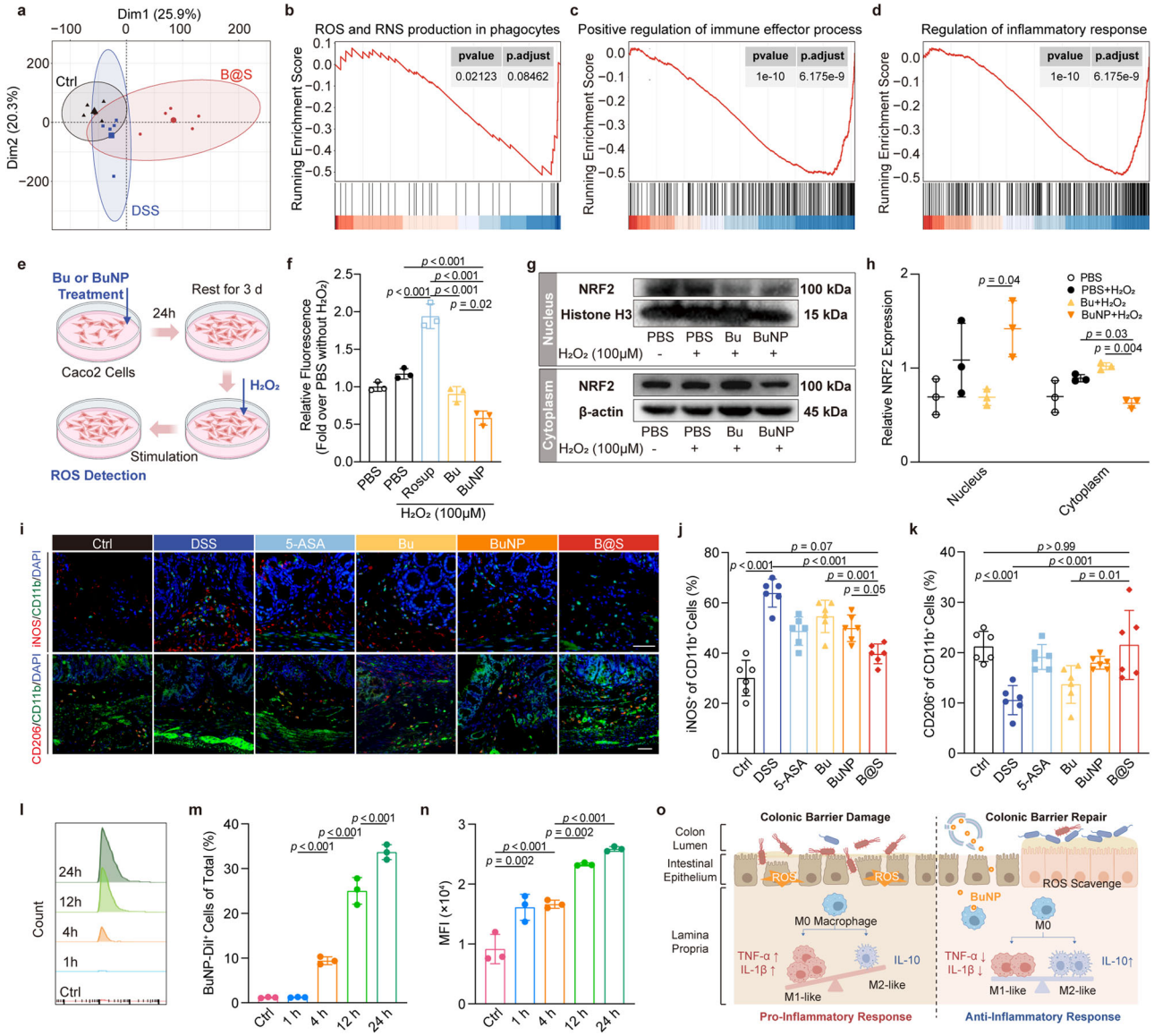

Fig. 5 | Regulation of redox balance and macrophage polarization by engineered postbiotics nanoparticles helped to protect the colonic barrier. **a**–**d** RNA sequencing data of colon tissues were processed by PCA (**a**, $n = 5$ mice), as well as GSEA (**b**–**d**, $n = 5$ mice). **e** Schematic test process of ROS scavenging capacity in vitro. Created in BioRender. https://BioRender.com/t60n948. **f** Antioxidative activity of Bu and BuNP under oxidative stress (100 μM H_2O_2) detected with fluorescence probe DCFH-DA ($n = 3$ biologically independent samples). Rosup (50 mg mL^{-1}) was a positive control of the test. **g**, **h** Representative Western blotting images (**g**) and semi-quantification (**h**, $n = 3$ biologically independent samples) of NRF2 in the nucleus and cytoplasm proteins of Caco2 cells. (**i**–**k**) Representative immunofluorescent staining images (**i**) and quantification of ratio of iNOS (red) and CD11b (green) double-positive cells to CD11b positive cells (**j**, $n = 6$ mice), as well as CD206 (red) and CD11b (green) double-positive cells to CD11b positive cells (**k**, $n = 6$ mice) on colon sections, counterstained by DAPI (blue). Scale bars, 50 μm. **l**–**n** The uptake of Dil-labeled-BuNP (BuNP-Dil) by THP-1 cells detected via flow cytometry (**l**), and analysis of the percentage of BuNP-Dil positive cells in all THP-1 cells (**m**, $n = 3$ biologically independent samples) as well as the mean fluorescent intensity of each cell (**n**, $n = 3$ biologically independent samples). **o** Schematic of the proposed combinational colon barrier protection mechanism of B@S. B@S scavenged ROS stimulation of epithelial cells and reversed polarization of macrophages in lamina propria from M1-like to alternatively M2-like phenotype. Created in BioRender. https://BioRender.com/z84q910. The numerical data in (**a**–**d**, **f**, **h**, **j**, **k**, **m**, **n**) are presented as mean ± s.d. A permutation test (**b**–**d**) or one-way ANOVA with Tukey's post-test for multiple comparisons (**f**, **h**, **j**, **k**, **m**, **n**) was made for statistical significance analysis. These experiments (**g**, **i**, **l**) were repeated three times independently with similar results. Source data are provided as a Source Data file.

viability[32]. Moreover, flow cytometry indicated that Caco2 cells had negligible uptake of BuNP (Supplementary Fig. 9b–d). Next, we performed RNA sequencing (RNA-seq) by using colon tissues from different treatment groups to get deep insight into the underlying mechanisms. Principal component analysis (PCA, Fig. 5a) showed that the DSS group had different gene expression from the Ctrl group, and B@S treatment altered that of the DSS group. Gene set enrichment analysis (GSEA) validated that the B@S-treated group down-regulated expression of genes for ROS and reactive nitrogen species (RNS) production in phagocytes (Fig. 5b), positive regulation of the immune system (Fig. 5c), and inflammatory response (Fig. 5d), compared to DSS group. Therefore, we observed the therapeutic mechanism of B@S from the sight of redox balance, immune regulation, and inflammation control in further experiments.

In pathological conditions like colitis, overproduction of ROS leads to prolonged oxidative stress status and disrupts intestinal homeostasis[33]. To test the ability of BuNP to scavenge ROS and suppress ROS-induced oxidative stress, intracellular ROS generation of

Caco2 cells was detected using a fluorescent probe 2′,7′-dichlorofluorescein diacetate (DCFH-DA) as the indicator (Fig. 5e). It was observed that cells treated with positive control Rosup or 100 μM hydrogen peroxide (H_2O_2) exhibited obvious ROS fluorescence signal. BuNP treatment significantly reduced intracellular ROS, while Bu had less effect (Fig. 5f). We then explored the antioxidative mechanism of BuNP. It is recognized that nuclear factor erythroid 2-related factor 2 (NRF2) is synthesized but rapidly degraded through the proteasome system in an unstressed environment. However, NRF2 can translocate to the nucleus under oxidative stresses and inhibit the expression of proinflammatory cytokine genes, like inducible nitric oxide synthase (iNOS)[34]. Herein, we detected the protein levels of NRF2 after Caco2 cells were exposed to 100 μM H_2O_2; western blotting showed that the BuNP treatment group showed significantly down-regulated NRF2 levels in the cytoplasm and up-regulated NRF2 levels in the nucleus compared to with Bu treatment group (Fig. 5g, h), which indicated the translocation of NRF2. Under oxidative conditions, the Bu group exhibited a higher mRNA level of iNOS than the BuNP group, which prompted that direct using of butyrate might bring oxidative insults to cells (Supplementary Fig. 9e and Supplementary Table 1). These results suggested that nano-form butyrate (BuNP) protected the cell viability and promoted ROS scavenging ability of epithelium cells, compared to the use of butyrate.

Butyrate has been reported as an immune regulatory factor in treating various inflammatory diseases[35]. Increased inflammatory (M1-like) and decreased anti-inflammatory (M2-like) phenotypes of macrophages are commonly observed in the inflammatory colon tissues of ulcerative colitis (UC) patients, and the disbalancing of M1-like and M2-like phenotypes correlates with the disease progression[36]. Herein, to investigate the role of B@S in regulating macrophage polarization in vivo, CD11b, iNOS, and CD206 were detected in the colon tissue of treated mice via IF staining. As shown in Fig. 5i–k, the decreased number of $CD11b^+$ / $iNOS^+$ double-positive cells (inflammatory makers) and the increased number of $CD11b^+$ / $CD206^+$ double-positive cells (anti-inflammatory makers) in the colon tissues indicated the M1-like to M2-like transformation of macrophages in vivo. Furthermore, the intake capacity of macrophages toward BuNP was evaluated through flow cytometry analysis in vitro; the result showed that THP-1 cells could uptake BuNP with time-dependent behavior (Fig. 5l–n). We also verified that BuNP suppressed M1-like macrophages secreted pro-inflammatory cytokines, including interleukin 1 beta (IL-1β) (Supplementary Fig. 10a) and TNF-α (Supplementary Fig. 10b), while promoting CD206 expression (Supplementary Fig. 10c), and release of anti-inflammatory cytokines IL-10 (Supplementary Fig. 10d) (primer gene sequences provided in Supplementary Table 1). The modulation form of BuNP toward macrophage polarization is shown in Supplementary Fig. 10e.

In summary, the cumulation of BuNP in inflamed colon tissue restored intestinal homeostasis by promoting the ROS scavenging ability of epithelium cells and regulating the M2-like polarization of macrophages. These together contributed to the effectiveness of B@S in treating DSS-induced colitis as well as alleviating systemic inflammation status (Fig. 5o).

Engineered postbiotics nanoparticles restored post-menopause-induced osteoporosis through the gut-bone axis

The therapeutic outcomes appeared significant in the GI and skeletal systems after treating B@S in DSS-induced mice by protecting the intestinal barrier and modulating systemic inflammation. In this case, we wondered if it had a similar effect on treating postmenopausal-induced primary osteoporosis. To set up a postmenopausal osteoporosis animal model, bilateral ovariectomy (OVX) was conducted on 6-to-8-week-old C57BL/6 N female mice. OVX mice were treated with Bu or B@S every three days by oral gavage (Fig. 6a). OVX mice showed apparent elevation of body weight during the experiment, while mice treated with B@S displayed a more gradual weight gain as the Sham group (Supplementary Fig. 11a). Next, to evaluate whether B@S obtain the therapeutic effect to protect bone loss in OVX mice, we used μCT analysis and the result showed that the B@S treatment was capable of increasing the bone mass when compared with OVX and Bu-treated OVX group (Fig. 6b), with the quantitative statistics of BV/TV (Fig. 6c), BS/BV (Fig. 6d), Tb.Th (Supplementary Fig. 11b) and Tb.Sp (Supplementary Fig. 11c). H&E staining (Fig. 6e) also showed that the B@S treatment increased the bone volume compared to OVX and Bu-treated OVX group, which was consistent with the μCT results. A similar osteoblast-osteoclast pattern was observed in the B@S-treated OVX group as the DSS model, in which a higher number of OCN-positive osteoblasts shown by IF staining (Fig. 6f, g) and a lower number of TRAP-positive osteoclasts shown by TRAP staining (Fig. 6h, i) on the surface of trabecular bone. Changes in the serum levels of bone turnover markers were examined further to assess the anti-osteoporosis effect of B@S on OVX mice. Consistent with a previous report[37], the bone formation makers, OCN and P1NP, were reduced, while the bone resorption maker, CTX-I, was elevated in OVX mice (Supplementary Fig. 12a–c). B@S treatment helped decrease CTX-I levels and elevate P1NP and OCN levels to the normal range (Supplementary Fig. 12a–c). To confirm this observation, the calcein-labeling assay showed that B@S treatment increased new bone formation and mineralization in OVX mice (Supplementary Fig. 12d–g). The OVX-induced reduction of maximum load and flexural strength of the femurs can also be reversed after B@S treatment (Supplementary Fig. 12h, i). These results illustrated that B@S could induce obvious impacts on promoting osteoblastic bone formation and inhibition of osteoclastic bone resorption in OVX mice. Previous studies concluded that estrogen deficiency impaired intestinal integrity, accompanied by an elevation of systemic inflammation, disrupting bone metabolism[37]. Thus, we analyzed the intestinal barriers of B@S-treated OVX mice histologically (Fig. 6j, k). The H&E staining showed that the histomorphology and HAI of colon tissues were not apparently altered in either of the OVX or B@S treatment groups (Fig. 6l). Next, we detected the tight junction of colonic epithelium via IF staining, the OVX group showed a significant decrease of claudin-1 (Fig. 6m) and ZO-1 (Fig. 6n), which indicated impaired intestinal integrity as previous reported[37]. Notably, the B@S treatment was able to rescue the levels of claudin-1 and ZO-1 significantly. Accompanied by restoring intestinal integrity, we also found that B@S treatment could rescue the balance of M1-like/M2-like macrophages in OVX mice. The IF staining analysis showed that OVX mice obtained a disbalancing of macrophage polarization, B@S treatment helped to decrease the number of $CD11b^+$ / $iNOS^+$ double-positive cells and increase the number of $CD11b^+$ / $CD206^+$ double-positive cells in the colon tissues indicated the M1-like to M2-like transformation of macrophages in vivo (Supplementary Fig. 13a–c). The flow cytometry analysis showed the same trends, and the ratio of CD86/CD206 in the OVX colon tissue decreased after B@S treatment (Supplementary Fig. 13d–f). From the aspect of system assessment, B@S treatment significantly decreased the serum level of LPS (Fig. 6o) and pro-inflammation cytokine TNF-α (Fig. 6p) compared with the OVX group. Besides, a lower concentration of pro-inflammation cytokine IL-1β was also observed in the B@S-treated group but with no significance (Fig. 6q).

Oral administration of engineered postbiotics nanoparticles restored the intestinal integrity of OVX mice, decreasing the level of LPS and pro-inflammatory cytokines in the systemic circulation. The anti-inflammatory capacity extends the usage of postbiotics nanoparticles not only to alleviate gut-derived inflammation-induced osteoporosis but also to obtain a positive effect on post-menopause-induced osteoporosis.

Discussion

Our study found that the gastrointestinal barriers were damaged, followed by activation of systemic inflammation in DSS-induced colitis mice, significantly reducing bone mass. With the supplement of

https://doi.org/10.1038/s41467-024-55263-1

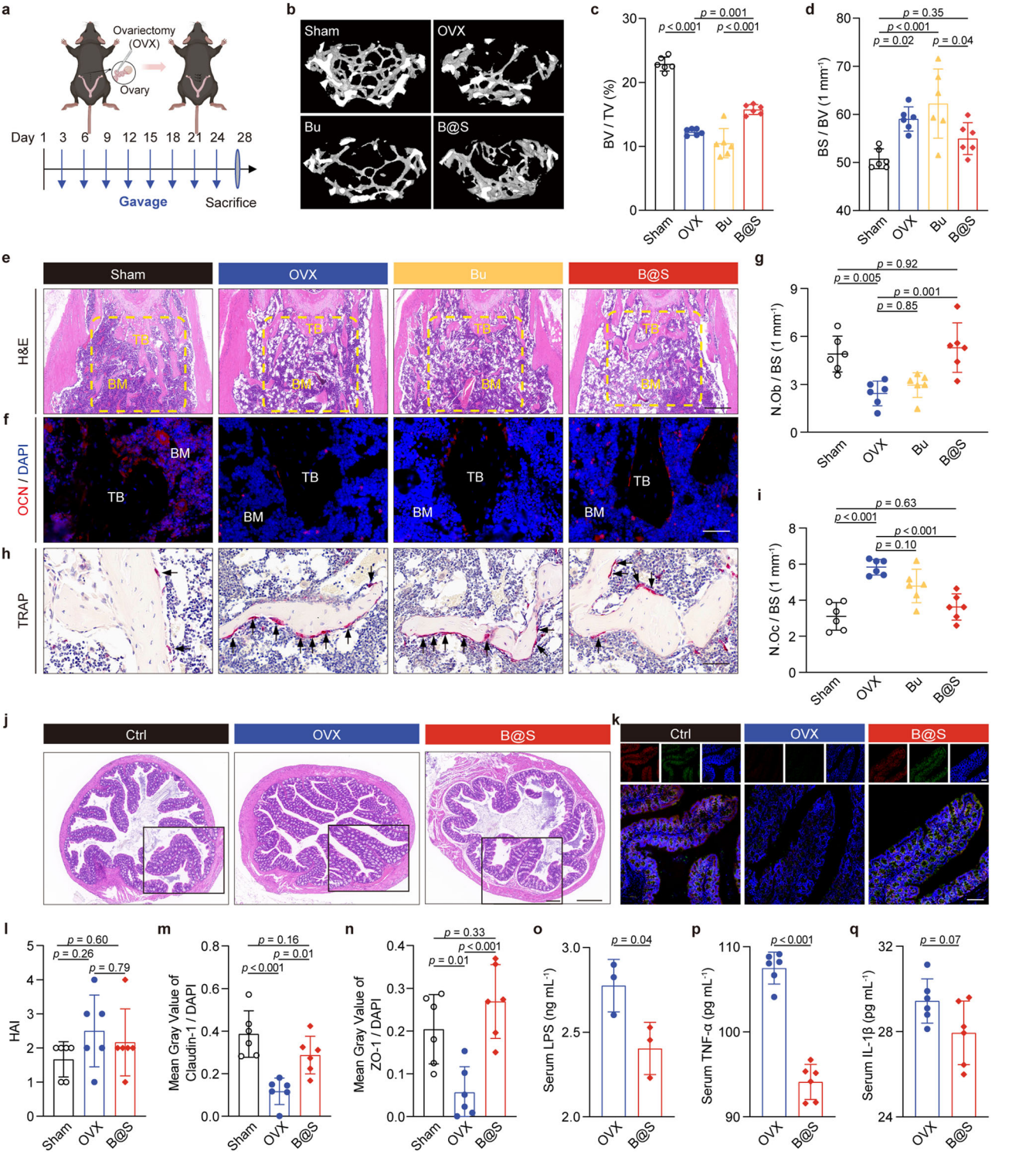

Fig. 6 | Engineered postbiotics nanoparticles restored post-menopause-induced osteoporosis through the gut-bone axis. a Schematic illustration of OVX-induced-osteoporosis therapeutic study. C57BL/6 N mice underwent ovariectomy and were treated with Bu or B@S twice a week for 4 weeks. Femurs of mice were collected after sacrifice. Created in BioRender. https://BioRender.com/d59i219. **b**–**d** Representative 3D restoration images (**b**), quantification of BV/TV (**c**, $n = 6$ mice) and BS/BV (**d**, $n = 6$ mice) of distal femurs, as scanned by μCT. **e** Representative H&E staining images (scale bar, 300 μm). TB, trabecular bone. BM, bone marrow. **f**, **g** Representative IF staining images of OCN (red) and DAPI (blue) (scale bar, 50 μm) (**f**) and analysis of OCN-positive osteoblast number/bone surface ratios (N.Ob/BS) (**g**, $n = 6$ mice). **h**, **i** Representative TRAP staining images (scale bar, 50 μm) (**h**) and analysis of osteoclast number/bone surface ratios (N.Oc/BS) (**i**, $n = 6$ mice). Black arrows on (**h**) pointed to TARP-positive osteoclasts. **j**–**n** Representative histological staining images of colon sections in mice. H&E staining images (scale bars, 500 μm, and 125 μm for enlarged images) were on paraffin-embedded sections (**j**) and calculation of HAI (**l**, $n = 6$ mice), as well as IF staining images (scale bar, 125 μm) (**k**) and semi-quantification of claudin-1 (red) (m, $n = 6$ mice), ZO-1 (green) (n, $n = 6$ mice) and DAPI (blue) were on frozen sections. DAPI, 4,6-diamidino-2-phenylindole. **o**–**q** The concentration of LPS (**o**, $n = 3$ mice), TNF-α (**p**, $n = 6$ mice), and IL-1β (**q**, $n = 6$ mice) in serum of OVX and B@S group measured via ELISA. The numerical data in (**c**, **d**, **g**, **i**, **l**–**q**) are presented as mean ± s.d. A one-way ANOVA with Tukey's post-test for multiple comparisons (**c**, **d**, **g**, **i**, **l**–**n**) or two-sided unpaired Student's *t* test (**o**–**q**) was made for statistical significance analysis. These experiments (**b**, **e**, **f**, **h**, **j**, **k**) were repeated three times independently with similar results. Source data are provided as a Source Data file.

postbiotics nanoparticles by oral delivery, the intact intestinal barrier was restored, and the systemic inflammation was suppressed, which led to the alleviation of bone loss in colitis mice. We extended the use of postbiotics nanoparticles in treating postmenopausal osteoporosis. The intestinal barrier integrity of OVX mice is significantly improved, and the proinflammatory cytokines in the circulation are inhibited after the postbiotics nanoparticles treatment, followed by the elevation of bone mass.

Bone has long been linked with the GI system due to the requirement for nutrient absorption to maintain bone homeostasis; more recently, studies indicated a variety of additional mechanisms involved, including immune regulation and microbiota[38,39]. Several studies revealed that patients with IBD obtain significant decreases in bone mass and changes in bone architecture due to the chronic inflammatory disorder[12,13,40], while the OP patients exhibit an inflamed intestinal characteristic and variation of gut microbiota[41], these results indicating an interplay relationship between the gut and bone system which still need further study. Developing targeted therapies for osteoporosis in IBDs is needed as the current clinical management has far reached satisfactory[42]. Here, we verified that B@S repaired intestinal epithelial and immune barriers and regulated dysbiosed gut microbiome to alleviate DSS-induced colitis. Shin et al.[27]. developed path-mimetic gut inflammation-on-a-chip to identify the trigger of intestinal inflammation in DSS-induced colitis. The results suggested that an intact epithelial barrier is a prerequisite to maintaining "homeostatic tolerance" in response to physiological host-gut microbiome cross-talks. In our study, B@S could repair damaged epithelial barrier, proved via ZO-1 and claudin-1 levels. This may become a key determinant for blocking subsequent ROS generation and proinflammatory cytokine production, which the decrease of serum LPS, TNF-α, and IL-6 levels of B@S-treated mice could partly demonstrate. However, the etiology and underlying mechanisms of IBD-induced osteoporosis still need further systemic exploration, as the bone metabolism in IBD patients should be more complicated.

Trillions of microorganisms inhabit the gastrointestinal tract and coevolve with the host, forming mutually beneficial relationships[43]. These symbiotic microorganisms, known as gut microbiota, regulate host homeostasis in numerous ways. It is clear that the gut microbiota influences the local intestinal immune response and contributes to the function of distal organs, including joints[44], livers[45], periodontal tissues[46], and central nerve systems[47]. Thus, manipulating the microbiome or its functional metabolites may afford opportunities for systemic diseases, including osteoporosis. Recent studies verified the positive influence of probiotics[38], functional microbe[39], and SCFA[15] to preserve systemic bone mass by gut microbiota alteration. Butyrate is a type of SCFA with anti-inflammatory properties. The gradual release of butyric acid helps modulate the local gut environment, which plays a crucial role in regulating the activity and polarization of macrophages[48,49]. However, obtaining an efficient therapeutic outcome is hard as the delivery system cannot achieve localized treatment, which reduces systemic toxicity[50]. Nanotechnology has been used in oral delivery systems to enhance uptake into inflamed colon tissue further. Several studies tried to solve this problem via different formulas, such as polyvinyl butyrate[51] and polymeric micelles releasing butyrate[52]. The stability of polyvinyl butyrate synthesized by Mu et al.[51] was only tested in constant pH 7.4 solutions, which did not reach the pH in gastric acid. In our oral delivery core-shell system, with the protection of the alkaline-responding ability of shellac, B@S was kept stable at pH 1.5 and started to resolve at pH 7.4. Wang et al.[52] synthesized two polymeric micelles releasing butyrate with neutral (NtL-ButM) or negative (Neg-ButM) charge. B@S also obtained a negative charge as Neg-ButM, which may help accumulate more B@S at positively charged epithelium lesion surfaces. Moreover, the fluorescent signals were below the detection limit in both of the major organs and bone tissue, confirming the colon-targeting and controlled release ability of B@S within 48 h, indicating more efficiency of the drug in modulating the local inflamed colon environment.

In conclusion, the postbiotics nanoparticles we designed obtained a core-shell structure that helped to transport butyrate along the distal intestinal tract. This achieved the controlled release of butyrate to prevent toxicity of rapid increase of butyrate luminal concentration. Consequently, accumulation of BuNP in inflamed colon tissue restored intestinal homeostasis through the regulation of redox balance, macrophage polarization, and gut microbiome; these together contributed to the effectiveness of postbiotics nanoparticles in treating DSS-induced colitis and alleviating systemic inflammation status. The control of systemic inflammation finally benefited the recovery of bone loss. Moreover, we extended the utility of postbiotics nanoparticles in the treatment of post-menopause osteoporosis, the integrity of intestinal barriers of OVX mice improved, and proinflammatory cytokines in the circulation can also be significantly inhibited, followed by the elevation of bone mass. Our study carried out therapeutic strategies for treating osteoporosis, especially IBD-induced bone loss, through the insight of regulating the gut-bone axis and highlighted the importance of intestinal barrier integrity in maintaining bone homeostasis.

Methods

Synthesis of BuNP

Polyvinyl Butyrate (PVBu) was produced by radical polymerization, and BuNP was made using the previously described oil-in-water emulsion solvent evaporation process[51]. Briefly, 100 mL of toluene (Wako Pure Chemical Industries, Japan, catalog No. 203-18465) solution containing 0.28 g azobisisobutyronitrile (AIBN) (J&K Scientific, China, catalog No. 614752) and 20 g vinyl butyrate (Tokyo Chemical Industry, Japan, catalog No. B0765) were added to a 200 mL round-bottom flask. The solution was then septa-sealed and nitrogen-purged for 30 min. After that, the flask was moved to a water bath heated to 50 °C for 48 h of polymerization. Dialyzing the polymerization solution against methanol (Wako Pure Chemical Industries, Japan, catalog No. 133-15355) took 48 h. Following dialysis, methanol was extracted by rotary evaporation and lyophilized to get PVBu.

A 100 mL flask was filled with 2.0 mL of a toluene solution containing 0.4 g mL^{-1} of PVBu and 20 mL of an aqueous solution containing 100 mg calcitriol (Cayman Chemical, USA, catalog No. 71820) and 5% (w/v) Pluronic F-127 (Sigma-Aldrich, USA, catalog No. P2443). The two phases were homogenized for 10 min at 1,000 rpm stirring speed and then subjected to 5 min of probe sonication (20% power, 20 kHz, 20 W). Toluene was evaporated at 300 rpm stirring speed overnight and then stored at 4 °C before usage to produce BuNP devoid of organic solvent.

Preparation of shellac hydrogel and B@S

To make the Shellac-COONa, 8.0 g shellac (Shanghai Acmec Biochemical Technology Co., Ltd., China, catalog No. S30690) was dissolved in 100 mL of distilled water containing 3.0 g Na_2CO_3, and the liquid was stirred until it turned deep-purple black. After that, 11.5 g gluconic acid lactone (GDL) (Aladdin Industrial, China, catalog No. G106879) was added to the solvent and well-mixed for 5 min using a magnetic stirrer. After the liquid became totally opaque, it was centrifuged for 15 min at 3000 × *g*, to remove the supernatant. The gel-like shellac was then collected and lyophilized for subsequent use[53].

BuNP-loaded shellac nanoparticles were prepared using a modified double-emulsion (water-in-oil-in-water) solvent evaporation/diffusion technique. Briefly, 8.0 mL of an organic combination of dichloromethane (Beijing InnoChem Science & Technology Co., Ltd., China, catalog No. G00001) and methanol (v/v, ratios of 5:3) was used to dissolve 50.0 mg of lyophilized shellac. After that, an ultrasonic homogenizer sonicator was used to sonicate a mixture of 0.2 mL of BuNP solution and 2.0 mL of shellac solution for 3 min in a cold bath.

After adding 2.0 mL of a 1% (w/v) sodium cholate (Macklin, China, catalog No. S821473) solution, the mixture was homogenized for 5 min in an ice bath. The resultant emulsion was slowly added to a solution of 0.5% (w/v) sodium cholate in 10.0 mL, and the mixture was stirred for 10 min at room temperature. The remaining organic solvents were evaporated to get rid of the dichloromethane. The suspended nanoparticles in the emulsion were collected by centrifuging at 11,000 × *g* for 15 min at room temperature. The supernatant was discarded, and the nanoparticles were resuspended in distilled water.

Characterization of B@S

The size and zeta potential of the collected nanoparticles in liquid suspension was measured by a Zeta Sizer Nano Series analyzer (Malvern Instrument, UK, software version 8. 01. 4906). The dynamic light scattering method was used to assess particle size, and the Z-Ave value was reported as the mean diameter of nanoparticles. The zeta potential was measured *via* the electrophoretic light scattering method.

To test the stability of nanoparticles, 10 mg of shellac nanoparticles were placed in a dialysis bag and immersed in 50 mL of various pH PBS buffer. The dialysis system was set up on a 200-rpm rotary shaker. The experiment lasted 4 h and was carried out at a constant temperature of 37 °C. Samples were taken at 4 h and then transferred to a specific cell. The particle size of the nanoparticles was determined using DLS by Zeta Sizer Nano Series analyzer (Malvern Instrument, UK, software version 8. 01. 4906).

In vitro drug release study of B@S

B@S nanoparticles were encapsulated in a dialysis bag with a 3500 Da molecular weight cut-off. The sealed bag was immersed in a buffer solution mimicking simulated gastric fluid (SGF, pH 1.5) and simulated intestinal fluid (SIF, pH 7.4) at 37 °C within an orbital shaker set to 120 rpm. At specified intervals, buffer samples were collected and replaced with an equal volume of fresh buffer to maintain consistent conditions. The collected samples were analyzed using high-performance liquid chromatography (HPLC) with a C18 column. The analysis employed an isocratic elution mobile phase of water acidified with 0.1% phosphoric acid and acetonitrile in an 80:20 ratio. Detection was performed at a wavelength of 206 nm, and the cumulative percentage release of sodium butyrate was calculated based on these measurements.

Animals

Female C57BL/6 N mice (6-to-8-week-old) were purchased from Beijing Vital River Laboratory Animal Technology Co., Ltd., China. All animal experiments in this study were approved by the Institutional Animal Care and Use Committee of Peking University (approval number LA2022403). Mice were housed in the specific pathogen-free (SPF) facility with a 12 h/12 h light/dark cycle at 25 °C and 60% humidity. They were allowed a sterile diet and autoclaved water ad libitum for 1 week before experiments.

In vivo biodistribution of B@S

6-to-8-week-old female C57BL/6 N mice were used to evaluate the in vivo biodistribution of B@S. In the synthesis process of BuNP, a toluene solution containing 0.4 g mL^{-1} PVBu was added with 10 μg mL^{-1} Rhodamine B (Aladdin Industrial, China, catalog No. R104960) to label nanoparticles with fluorescence. Then, the Rhodamine B-labeled BuNP (BuNP-Rhodamine B) was loaded in shellac ((BuNP-Rhodamine B)@Shellac). The mice were orally gavaged (BuNP-Rhodamine B)@Shellac (equal amount of 1.75 g kg^{-1} butyrate) and sacrificed after 0 (Ctrl), 1, 4, 24 and 48 h of gavage, respectively. Major organs, including gastrointestinal (GI) tracts, heart, liver, spleen, lung, and kidney, were dissected and rinsed with PBS twice. The fluorescence signal was detected using the IVIS Spectrum imaging system (PerkinElmer, USA). Living Image software (PerkinElmer, USA, version 4.3.1) was used to quantify the radiant efficiency of acquired images.

Establishment and treatment of DSS-induced acute colitis model

Female C57BL/6 N mice (6-to-8-week-old) of all colitis groups were provided with water containing 2% (w/v) DSS (MP Biomedicals, USA, catalog No. 160110) for 8 days to induce acute colitis, while Ctrl group received free water. Body weight-matched colitis mice were randomly sorted into different treatment groups. From the day starting drinking DSS water, colitis mice were orally gavaged with sterile double distilled water (ddH_2O), 5-ASA (0.25 mmol kg^{-1} d^{-1}, Solarbio, China, catalog No. A6900), butyrate (Bu) (1.75 g kg^{-1} d^{-1}, J&K Scientific, China, catalog No. 479725), BuNP (equal amount of 1.75 g kg^{-1} d^{-1} butyrate) and B@S (equal amount of 1.75 g kg^{-1} d^{-1} butyrate) every other day for 4 times. During the experiment, mice's body weights were recorded daily, and the mice were sacrificed on the 8th day. The length of the colon was measured immediately after dissection. DAI was evaluated according to the severity of body weight change, diarrhea, and bleeding, as described previously[54]. Briefly, body weight loss of none, 1–5%, 5–10%, 10–15%, or more than 15% was counted as 0, 1, 2, 3, or 4 points, separately. No diarrhea, diarrhea with loose stools, or watery diarrhea was counted as 0, 2, or 4 points. No, slight or gross bleeding was counted as 0, 2, or 4 points. The sum of scores of these three parameters made up the DAI.

Establishment and treatment of DSS-induced colitis complicated with osteoporosis model

Female C57BL/6 N mice (6-to-8-week-old) of all colitis groups were provided water containing 2% (w/v) DSS during the 1st week. The concentration of DSS was adjusted to 1% (w/v) during the 2nd week[22]. The Ctrl group received free water for two weeks. Body weight-matched colitis mice were randomly sorted into different treatment groups. From the day starting drinking DSS water, colitis mice were orally gavaged with sterile ddH_2O, 5-ASA (0.25 mmol kg^{-1} d^{-1}), Bu (1.75 g kg^{-1} d^{-1}), BuNP (equal amount of 1.75 g kg^{-1} d^{-1} butyrate) and B@S (equal amount of 1.75 g kg^{-1} d^{-1} butyrate) every other day for 6 times. The mice were sacrificed on the 14th day.

Micro-computed tomography (μCT) examination and analysis

Femurs of mice were dissected and fixed in 4% paraformaldehyde (PFA) (Solarbio, China, catalog No. P1110) for two days and then scanned by Skyscan 1276 (Bruker, USA, software version 1.8). Images were acquired with a spatial resolution of 6 μm (50 kV voltage, 200 μA current). μCT images were reconstructed into three-dimensional (3D) images and analyzed by Nrecon (version 2.2.0.6), DataViewer (version 1.7.0.1), CT Analyzer (version 1.20.8.0), and Ctvox (version 3.3.0.0) software (Bruker, USA). For analysis, the region of interest (ROI) started from 0.7 mm beneath the growth plates and had a total height of 0.5 mm. 3D reconstruction images of ROIs presented a mass of trabecular bone. BV/TV, BS/BV, Tb.Th and Tb.Sp were calculated within the ROIs.

Histological staining of colon and femur

The proximal part of the colon or the entire femur was fixed in 4% PFA for two days. Femurs were washed and decalcified in a decalcifying agent (Solarbio, China, catalog No. E1171) for four weeks. Colons or decalcified femurs were dehydrated, embedded in paraffin, and cut into 3 μm-thick sections for H&E staining as well as TRAP staining. Fixed colon or decalcified femur tissues were frozen in optimal cutting temperature compound (OCT) (Sakura Finetek USA Inc., USA, catalog No. 4583) and cut into 8 μm-thick sections for IF staining. Colon tissues were cut transversally, while femur tissues were cut longitudinally.

For IF staining, sliced sections were permeabilized and blocked with PBS containing 5% (w/v) bovine serum albumin (BSA) (Solarbio, China, catalog No. A8020) and 0.3% (v/v) Triton X-100 (Beyotime,

China, catalog No. ST1722) for 1 h, then incubated with primary antibodies overnight at 4 °C. The primary antibodies included anti-claudin-1 (Abcam, UK, catalog No. ab307692; clone EPR25359-48; lot No. 1068101-27; dilution 1:100), anti-ZO-1 (Santa Cruz Biotechnology, USA, catalog No. sc-33725; clone R40.76; lot No. B0724; dilution 1:200), anti-OCN (Santa Cruz Biotechnology, USA, catalog No. sc-390877; clone D-11; lot No. A0524; dilution 1:200), anti-CD11b (Abcam, UK, catalog No. ab8878; clone M1/70; lot No. 1058850-15; dilution 1:100), anti-iNOS (Abcam, UK, catalog No. ab178945; clone EPR16635; lot No. 1001367-53; dilution 1:500) and anti-CD206 (Cell Signaling Technology, USA, catalog No. 24595 T; clone E6T5J; lot No. 3; dilution 1:500) antibodies. After washing with PBS 3 times, sections were incubated with corresponding fluorescence-conjugated secondary antibodies (ZSGB-BIO, China) for 1 h at room temperature. Sections were washed with PBS 3 times and sealed with an anti-fading mounting medium containing 4′,6-diamidino-2-phenylindole (DAPI) (Solarbio, China, catalog No. S2110). Fluorescence images were taken using Pannoramic SCAN II (3D HISTECH, Hungary, software version 3.0.7) and analyzed by Image J software (National Institutes of Health, USA, version 1.54 f).

Histomorphometric analysis of femur

Image J software performed histomorphometric analysis of distal femurs. Trabecular bone volume was analyzed using H&E staining images. We measured the number of osteoblasts per bone surface (N.Ob/BS) on IF staining images of OCN and the number of osteoclasts per bone surface (N.Oc/BS) on TRAP staining images. Bone surface (BS) values were represented with trabecular bone perimeters on these two-dimensional images.

Histological analysis of colon

As previously described, H&E staining images of colons were used to measure HAI[54]. Briefly, HAI was calculated as the sum of epithelial damage and infiltration score. Epithelial damage score was counted as 0 with no damage, 1 or 2 with minimal or extensive loss of globet cells, 3 with extensive loss of globet cells and minimal loss of crypts, or 4 with extensive loss of crypts. Infiltration score was counted as 0 with no infiltration, 1 with infiltration around crypt bases, 2 with infiltration in muscularis mucosa, 3 with extensive infiltration in muscularis mucosa with edema, or 4 with infiltration of submucosa. Semi-quantification was conducted by the mean gray value of the fluorescence signal of claudin-1 and ZO-1 proteins per intestinal villi fold over DAPI on IF images. The percentage of iNOS and CD11b double-positive cells, as well as CD206 and CD11b double-positive cells, was calculated on multi-stained fluorescence images.

Fecal microbiome 16S rRNA sequencing and analysis

Feces collected from the cecum of mice were frozen in liquid nitrogen. Microbiome 16S rRNA sequencing of feces was carried out in Shanghai Majorbio Bio-pharm Biotechnology Co., Ltd. (China). Briefly, genomic DNA was extracted and detected by 1% agarose gel electrophoresis. PCR was carried out using TransStart Fastpfu DNA Polymerase (TransGen Biotech, China) in PCR9700 (ABI, USA). The PCR products were quantified via the QuantiFluor -ST Blue fluorescence quantification system (Promega, China). Illumina library construction was done using TruSeq DNA Library Prep Kits (Illumina, USA). Library quality control was performed before sequencing on an Illumina platform at Shanghai Majorbio Bio-pharm Technology Co., Ltd. PE reads sequenced by Illumina were first spliced according to overlap, and the sequence quality was controlled and filtered. The sequencing data were analyzed online on the Majorbio Cloud Platform (www.majorbio.com).

Targeting metabolomics analysis of mice feces

During mice sample collection, feces in the cecum were frozen in liquid nitrogen. To test the concentration of SCFA in mice feces, targeting metabolomics of feces was carried out in Shanghai Majorbio Bio-pharm Biotechnology Co., Ltd. (China). Firstly, a standard solution of SCFA was prepared, including acetic acid, propanoic acid, and butanoic acid. Fecal samples (20 mg) were mixed with 800 µL 0.5% phosphoric acid, frozen, and ground for 3 min (50 HZ), then ultrasound for 10 min and centrifuged at 4 °C at 13,000 × *g* for 15 min. After centrifugation, 200 µL supernatant was collected and mixed with 200 µL n-butanol solvent for extraction. After vortexing for 10 sec, ultrasound at low temperature for 10 min, and centrifuging at 4 °C at 13,000 × *g* for 5 min, the supernatant solution was prepared and ready for testing. Detection was done using the gas chromatography/mass spectrometry (GC/MS) instrument (8890B-5977B, Agilent Technologies Inc. CA, USA) according to the manufacturer's instructions. The Masshunter software (Agilent Technologies Inc. CA, USA) was used to analyze data.

ELISA

To evaluate the concentration of serum cytokines, the whole peripheral blood obtained from mice was placed to clot overnight at 4 °C and then centrifuged at 1000 × *g* for 20 min, and the supernatant was serum. The concentration of LPS (Cloud-Clone Corp. Katy, China, catalog No. IEB526Ge), LTA (LifeSpan, China, catalog No. LS-F66490), TNF-α (Invitrogen, USA, catalog No. BMS607-3), IL-1β (Invitrogen, USA, catalog No. BMS6002-2), IL-6 (Invitrogen, USA, catalog No. BMS603-2) and IL-10 (Invitrogen, USA, catalog No. BMS614) in serum were detected using ELISA kits according to manufacturers' instructions. Briefly, the assay was based on a double-antibody sandwich method, and the absorbance of samples was measured at 450 nm using a microplate reader (Molecular Devices, USA).

RNA sequencing and analysis

When mice were euthanized, we washed thoroughly and frozen the medium part of colon tissues freshly in liquid nitrogen. Total RNA was extracted from the colon tissue via TRIzol Reagent (Invitrogen, USA, catalog No. 15596018CN) according to the manufacturer's instructions. High-quality RNA samples were selected by 5300 Bioanalysers (Agilent, USA) and ND-2000 (NanoDrop Technologies, USA) to construct an RNA sequencing library. RNA samples were submitted to Shanghai Majorbio Bio-pharm Biotechnology Co., Ltd. (China). According to the manufacturer's instructions, they performed RNA purification, reverse transcription, library construction, and sequencing with a NovaSeq 6000 sequencer (Illumina, USA). The fast with default parameters was used for trimming and quality control of the raw paired-end reads. Then, clean reads were separately aligned to the reference genome with orientation mode using HISAT2[55] software. The mapped reads of each sample were assembled by StringTie[56] in a reference-based approach. The transcripts per million reads (TPM) method was used to identify differential expression genes (DEGs) between two different samples and calculate the expression level of each transcript. Gene abundances were quantified using RSEM[57], and differential expression analysis was performed by the DEGseq[58] or DESeq2[59]. Functional enrichment analysis, including GO and KEGG, was conducted via Goatools and KOBAS. Principal component analysis (PCA) was also conducted.

For gene set enrichment analysis (GSEA), the gene sets for ROS and RNS production in phagocytes, positive regulation of the immune system, and inflammatory response were obtained from the GSEA online database. Our gene list of interest was then put into the GSEA software (http://www.broad.mit.edu/GSEA).

Cell culture

Caco2 cells (purchased from Cell Resource Center, Peking Union Medical College, catalog No. 1101HUM-PUMC000100) were cultured in minimum essential medium α (MEM α) (Gibco, USA, catalog No. 12571063), supplemented with 10% (v/v) fetal bovine serum (FBS)

(Gibco, USA, catalog No. A5256701) and 100 IU mL^{-1} penicillin-streptomycin (Gibco, USA, catalog No. 15140122). THP-1 cells (purchased from American Type Culture Collection, ATCC, catalog No. TIB-202) were cultured in Roswell Park Memorial Institute (RPMI) 1640 medium (Gibco, USA, catalog No. 11875093), supplemented with 10% (v/v) FBS and 100 IU mL^{-1} penicillin-streptomycin. All the cells were incubated at 37 °C in a humidified atmosphere of 5% carbon dioxide and 95% air.

Intracellular ROS measurement

Caco2 cells were seeded into a 24-well plate and cultured for 48 h. Then, cells were treated with Bu (3.5 mg mL^{-1}) or BuNP (equal amount of 3.5 mg mL^{-1} butyrate) for 24 h, then washed and cultured in media without Bu or BuNP for 24 h, or treated with Rosup for 30 min, followed by 2 h-treatment of 100 μM H_2O_2. The level of intracellular ROS was detected via a Reactive Oxygen Species Assay Kit (Solarbio, China, catalog No. CA1410) containing probe DCFH-DA according to the manufacturer's instruction. Briefly, cells were washed with warm PBS, and 500 μL growth medium with 10 μM DCFH-DA was added to each well. After incubating at 37 °C for 20 min, the fluorescent intensity was measured using a Multimode Plate Reader (PerkinElmer, USA).

Western blotting

Caco2 cells were cultured in six-well plates, treated with Bu (3.5 mg mL^{-1}) or BuNP (equal amount of 3.5 mg mL^{-1} butyrate) for 24 h, then washed and cultured in media without Bu or BuNP for 24 h, and followed by adding of 100 μM H_2O_2 for another 12 h. Then, the nucleus and cytoplasmic proteins were extracted via a nuclear extraction kit (Solarbio, China, catalog No. EX1470) according to the manufacturer's instructions. Protein concentration was determined via the BCA Protein Assay Kit (ThermoFisher Scientific, USA, catalog No. 23227). Equal samples from each group were loaded into the wells of SDS-PAGE gels and transferred to polyvinylidene fluoride (PVDF) membranes (Millipore, USA, catalog No. ISEQ00005). Membranes were blocked in 5% (w/v) BSA in Tris-buffered saline with Tween-20 (TBST) (Solarbio, China, catalog No. T1082) for 1 h at room temperature and incubated at 4 °C overnight with primary antibodies. The primary antibodies were anti-NRF2 (Proteintech, UK, catalog No. 16396-1-AP; lot No. 00110057; dilution 1:200), anti-histone H3 (Santa Cruz Biotechnology, USA, catalog No. sc-517576; clone 1G1; lot No. D2621; dilution 1:200) and anti-β-actin antibodies (Cell Signaling Technology, USA, catalog No. 3700S; clone 8H10D10; lot No. 18; dilution 1:1000). After washing with TBST, the membranes were incubated with peroxidase-conjugated secondary antibodies (ZSGB-BIO, China) for 1 h at room temperature and then with enhanced chemiluminescence kit (ThermoFisher Scientific, USA, catalog No. 32106) by ChemiDoc imaging system (Bio-Rad, USA).

Flow cytometry

To analyze the cellular uptake of BuNP by THP-1 cells in vitro, flow cytometry was performed. THP-1 cells were incubated in culture media with 100 ng mL^{-1} phorbol-12-myristate-13-acetate (PMA) (Sigma-Aldrich, USA, catalog No. P8139) for 48 h, washed with PBS, and cultured in media without PMA for 24 h, to differentiate into a macrophage-like phenotype. Then we prepared BuNP labeled with 1,1′-dioctadecyl-3,3,3′,3′-tetramethylindocarbocyanine perchlorate (DiI) (Beyotime, China, catalog No. C1036), namely BuNP-DiI, and added it (equal amount of 3.5 mg mL^{-1} butyrate) to differentiated THP-1 cells. Cells were collected after adding BuNP-DiI for 0 (Ctrl), 1, 4, 12, and 24 h, washed with PBS for 3 times, and resuspended in PBS to get single-cell suspension. Flow cytometry was carried out via flow cytometer (Beckman Colter, USA) and data were analyzed by CytExpert software (Beckman Colter, USA, version 2.6.0.105).

Establishment and treatment of ovariectomy (OVX) mice model

6-to-8-week-old female C57BL/6 N mice were randomly assigned to different groups, anesthetized, and subjected to either a sham surgery (Sham) or bilateral ovariectomy (OVX). Small dorsal incisions were made to the exposure location of ovaries. For the Sham group, ovaries were put back into peritoneal cavity without other operations directly after locating. For OVX treatment, oviducts were exposed and ligated before the remove of bilateral ovaries. Finally, the incisions of all groups were sutured. Operated mice in Bu- (OVX + Bu) or B@S-treated OVX (OVX + B@S) group were orally gavaged Bu (1.75 g kg^{-1} d^{-1}) or B@S (equal amount of 1.75 g kg^{-1} d^{-1} butyrate) twice weekly for another four weeks before sacrifice.

Statistical analysis

All data is presented as mean ± error bars (s.d.), and n is stated in figure legends. A two-sided unpaired Student's t test was used for comparisons between the two groups. A one-way analysis of variance (ANOVA) with Tukey's post-test or two-way ANOVA with the Geisser-Greenhouse correction was used to make multiple comparisons. A permutation test was used for gene set enrichment analysis of RNA sequencing data.

Reporting summary

Further information on research design is available in the Nature Portfolio Reporting Summary linked to this article.

Data availability

The microbial diversity sequencing data generated in this study have been deposited in the NCBI Sequence Read Archive (SRA) database under accession code PRJNA1171616. The RNA-seq data generated in this study have been deposited in the NCBI SRA database under accession code PRJNA1166419. The main data generated in this study are provided in the Supplementary Information/Source Data file. Source data is available for Figs. 2, 3, 4, 5 and 6 and Supplementary Figs. 1, 2, 3, 4, 5, 7, 8, 9, 10, 11, 12 and 13 in the associated source data file. Source data are provided in this paper.

References

1. NIH Consensus Development Panel on Osteoporosis Prevention, Diagnosis, and Therapy. Osteoporosis prevention, diagnosis, and therapy. *JAMA* **285**, 785–795 (2001).
2. Reid, I. R. & Billington, E. O. Drug therapy for osteoporosis in older adults. *Lancet* **399**, 1080–1092 (2022).
3. Compston, J. E., McClung, M. R. & Leslie, W. D. Osteoporosis. *Lancet* **393**, 364–376 (2019).
4. Kong, N. et al. An injectable self-adaptive polymer as a drug carrier for the treatment of nontraumatic early-stage osteonecrosis of the femoral head. *Bone Res.* **10**, 28 (2022).
5. Pedersen, A. B., Heide-Jorgensen, U., Sorensen, H. T., Prieto-Alhambra, D. & Ehrenstein, V. Comparison of risk of osteoporotic fracture in denosumab vs alendronate treatment within 3 years of initiation. *JAMA Netw. Open* **2**, e192416 (2019).
6. Gonzalez-Rodriguez, E., Aubry-Rozier, B., Stoll, D., Zaman, K. & Lamy, O. Increased risk of multiple spontaneous vertebral fractures at denosumab discontinuation must be taken into account. *J. Clin. Oncol.* **38**, 1641–1642 (2020).
7. Anastasilakis, A. D. et al. Clinical features of 24 patients with rebound-associated vertebral fractures after denosumab discontinuation: Systematic review and additional cases. *J. Bone Miner. Res.* **32**, 1291–1296 (2017).
8. Fixen, C. & Tunoa, J. Romosozumab: a review of efficacy, safety, and cardiovascular risk. *Curr. Osteoporos. Rep.* **19**, 15–22 (2021).
9. Pharmacologic Treatment of Primary Osteoporosis or Low Bone Mass to Prevent Fractures in Adults: A Living Clinical Guideline From the American College of Physicians. *Ann. Intern. Med.* **176**, 224-238 (2023).

10. Zaiss, M. M., Jones, R. M., Schett, G. & Pacifici, R. The gut-bone axis: how bacterial metabolites bridge the distance. *J. Clin. Invest.* **129**, 3018–3028 (2019).
11. Merlotti, D. et al. Bone fragility in gastrointestinal disorders. *Int. J. Mol. Sci.* **23**, 2713 (2022).
12. Tilg, H., Moschen, A. R., Kaser, A., Pines, A. & Dotan, I. Gut, inflammation and osteoporosis: basic and clinical concepts. *Gut* **57**, 684–694 (2008).
13. Ke, K. et al. Attenuation of NF-κB in intestinal epithelial cells is sufficient to mitigate the bone loss comorbidity of experimental mouse colitis. *J. Bone Miner. Res.* **34**, 1880–1893 (2019).
14. Salminen, S. et al. The international scientific association of probiotics and prebiotics (ISAPP) consensus statement on the definition and scope of postbiotics. *Nat. Rev. Gastroenterol. Hepatol.* **18**, 649–667 (2021).
15. Lucas, S. et al. Short-chain fatty acids regulate systemic bone mass and protect from pathological bone loss. *Nat. Commun.* **9**, 55 (2018).
16. Li, G. et al. Microbiota metabolite butyrate constrains neutrophil functions and ameliorates mucosal inflammation in inflammatory bowel disease. *Gut Microbes* **13**, 1968257 (2021).
17. Hinrichsen, F. et al. Microbial regulation of hexokinase 2 links mitochondrial metabolism and cell death in colitis. *Cell Metab.* **33**, 2355–2366.e2358 (2021).
18. Furusawa, Y. et al. Commensal microbe-derived butyrate induces the differentiation of colonic regulatory T cells. *Nature* **504**, 446–450 (2013).
19. Koh, A., De Vadder, F., Kovatcheva-Datchary, P. & Backhed, F. From dietary fiber to host physiology: Short-chain fatty acids as key bacterial metabolites. *Cell* **165**, 1332–1345 (2016).
20. Peng, L., He, Z., Chen, W., Holzman, I. R. & Lin, J. Effects of butyrate on intestinal barrier function in a Caco-2 cell monolayer model of intestinal barrier. *Pediatr. Res.* **61**, 37–41 (2007).
21. Yuan, Y. et al. Multiscale shellac-based delivery systems: From macro- to nanoscale. *ACS Nano* **15**, 18794–18821 (2021).
22. Guo, J. et al. Exosome-based bone-targeting drug delivery alleviates impaired osteoblastic bone formation and bone loss in inflammatory bowel diseases. *Cell Rep. Med.* **4**, 100881 (2023).
23. Zuo, L., Kuo, W. T. & Turner, J. R. Tight junctions as targets and effectors of mucosal immune homeostasis. *Cell. Mol. Gastroenterol. Hepatol.* **10**, 327–340 (2020).
24. Yu, T. et al. Inhibition of Tet1- and Tet2-mediated DNA demethylation promotes immunomodulation of periodontal ligament stem cells. *Cell Death Dis.* **10**, 780 (2019).
25. Odenwald, M. A. & Turner, J. R. The intestinal epithelial barrier: a therapeutic target? *Nat. Rev. Gastroenterol. Hepatol.* **14**, 9–21 (2017).
26. Schirmer, M., Garner, A., Vlamakis, H. & Xavier, R. J. Microbial genes and pathways in inflammatory bowel disease. *Nat. Rev. Microbiol.* **17**, 497–511 (2019).
27. Shin, W. & Kim, H. J. Intestinal barrier dysfunction orchestrates the onset of inflammatory host-microbiome cross-talk in a human gut inflammation-on-a-chip. *Proc. Natl. Acad. Sci. USA* **115**, E10539–E10547 (2018).
28. Ghosh, S. S., Wang, J., Yannie, P. J. & Ghosh, S. Intestinal barrier dysfunction, LPS translocation, and disease development. *J. Endocr. Soc.* **4**, bvz039 (2020).
29. Potrykus M., Czaja-Stolc S., Stankiewicz M., Kaska L., Malgorzewicz S. Intestinal microbiota as a contributor to chronic inflammation and its potential modifications. *Nutrients* **13**, https://doi.org/10.3390/nu13113839 (2021).
30. Kang, S. S., Sim, J. R., Yun, C. H. & Han, S. H. Lipoteichoic acids as a major virulence factor causing inflammatory responses via Toll-like receptor 2. *Arch. Pharm. Res.* **39**, 1519–1529 (2016).
31. Bott, K. N. et al. Lipopolysaccharide-induced bone loss in rodent models: A systematic review and meta-analysis. *J. Bone Miner. Res.* **38**, 198–213 (2023).
32. Hua, S., Marks, E., Schneider, J. J. & Keely, S. Advances in oral nano-delivery systems for colon targeted drug delivery in inflammatory bowel disease: selective targeting to diseased versus healthy tissue. *Nanomedicine* **11**, 1117–1132 (2015).
33. Xu, J. et al. Probiotic-inspired nanomedicine restores intestinal homeostasis in colitis by regulating redox balance, immune responses, and the gut microbiome. *Adv. Mater.* **35**, e2207890 (2023).
34. Cuadrado, A. et al. Therapeutic targeting of the NRF2 and KEAP1 partnership in chronic diseases. *Nat. Rev. Drug Discov.* **18**, 295–317 (2019).
35. Yang, W. et al. Intestinal microbiota-derived short-chain fatty acids regulation of immune cell IL-22 production and gut immunity. *Nat. Commun.* **11**, 4457 (2020).
36. Zigmond, E. et al. Ly6C hi monocytes in the inflamed colon give rise to proinflammatory effector cells and migratory antigen-presenting cells. *Immunity* **37**, 1076–1090 (2012).
37. Guo, M. et al. Lactobacillus rhamnosus GG ameliorates osteoporosis in ovariectomized rats by regulating the Th17/Treg balance and gut microbiota structure. *Gut Microbes* **15**, 2190304 (2023).
38. Tyagi, A. M. et al. The microbial metabolite butyrate stimulates bone formation via T regulatory cell-mediated regulation of WNT10B expression. *Immunity* **49**, 1116–1131 (2018).
39. Liu, J. H. et al. Extracellular vesicles from child gut microbiota enter into bone to preserve bone mass and strength. *Adv. Sci.* **8**, 2004831 (2021).
40. Ott, C. & Scholmerich, J. Extraintestinal manifestations and complications in IBD. *Nat. Rev. Gastroenterol. Hepatol.* **10**, 585–595 (2013).
41. Ding, K., Hua, F. & Ding, W. Gut microbiome and osteoporosis. *Aging Dis.* **11**, 438–447 (2020).
42. Soos, B. et al. Effects of targeted therapies on bone in rheumatic and musculoskeletal diseases. *Nat. Rev. Rheumatol.* **18**, 249–257 (2022).
43. Qin, J. et al. A human gut microbial gene catalogue established by metagenomic sequencing. *Nature* **464**, 59–65 (2010).
44. Zaiss, M. M., Joyce Wu, H. J., Mauro, D., Schett, G. & Ciccia, F. The gut-joint axis in rheumatoid arthritis. *Nat. Rev. Rheumatol.* **17**, 224–237 (2021).
45. Le, H. H., Lee, M. T., Besler, K. R. & Johnson, E. L. Host hepatic metabolism is modulated by gut microbiota-derived sphingolipids. *Cell Host Microbe* **30**, 798–808 (2022).
46. Kitamoto, S. et al. The intermucosal connection between the mouth and gut in commensal pathobiont-driven colitis. *Cell* **182**, 447–462 (2020).
47. Erny, D. et al. Host microbiota constantly control maturation and function of microglia in the CNS. *Nat. Neurosci.* **18**, 965–977 (2015).
48. Li, X. et al. Butyric acid ameliorates myocardial fibrosis by regulating M1/M2 polarization of macrophages and promoting recovery of mitochondrial function. *Front. Nutr.* **9**, 875473 (2022).
49. Yang, J. et al. RhoB affects colitis through modulating cell signaling and intestinal microbiome. *Microbiome* **10**, 149 (2022).
50. Raqib, R. et al. Efficacy of sodium butyrate adjunct therapy in shigellosis: a randomized, double-blind, placebo-controlled clinical trial. *BMC Infect. Dis.* **12**, 111 (2012).
51. Mu, Y. et al. Polyvinyl butyrate nanoparticles as butyrate donors for colitis treatment. *ACS Appl. Bio Mater.* **4**, 2335–2341 (2021).
52. Wang, R. et al. Treatment of peanut allergy and colitis in mice via the intestinal release of butyrate from polymeric micelles. *Nat. Biomed. Eng.* **7**, 38–55 (2023).
53. Li, K. et al. A tough self-assembled natural oligomer hydrogel based on nano-size vesicle cohesion. *RSC Adv.* **6**, 33547–33553 (2016).

54. Alex, P. et al. Distinct cytokine patterns identified from multiplex profiles of murine DSS and TNBS-induced colitis. *Inflamm. Bowel Dis.* **15**, 341–352 (2009).
55. Kim, D., Langmead, B. & Salzberg, S. L. HISAT: a fast spliced aligner with low memory requirements. *Nat. Methods* **12**, 357–360 (2015).
56. Pertea, M. et al. StringTie enables improved reconstruction of a transcriptome from RNA-seq reads. *Nat. Biotechnol.* **33**, 290–295 (2015).
57. Li, B. & Dewey, C. N. RSEM: accurate transcript quantification from RNA-Seq data with or without a reference genome. *BMC Bioinformatics* **12**, 323 (2011).
58. Wang, L., Feng, Z., Wang, X., Wang, X. & Zhang, X. DEGseq: an R package for identifying differentially expressed genes from RNA-seq data. *Bioinformatics* **26**, 136–138 (2010).
59. Love, M. I., Huber, W. & Anders, S. Moderated estimation of fold change and dispersion for RNA-seq data with DESeq2. *Genome Biol.* **15**, 550 (2014).

Acknowledgements

This work was financially supported by grants from the National Key R&D Program of China (2022YFA1206100 to T.Y., 2021YFC2400403 to B.H., 2023YFC2509903 to Y.W.), the Fundamental Research Center Project of the National Natural Science Foundation of China (T2288102 to G.N.), the National Natural Science Foundation of China (52473120 to B.H., 52373123 to T.Y., U21A2055 to B.H.), the Strategic Priority Research Program of Chinese Academy of Sciences (XDB36000000 to G.N.), the Beijing Municipal Science Technology Commission (Z211100002921066 to B.H.), the Young Elite Scientist Sponsorship Program by CAST (2021QNRC001 to T.Y.) and the Beijing Nova Program (202304584382 to R.Z.). We thank Luzheng Xu and Qilong Wang from the Peking University Medical and Health Analysis Center for their assistance with Micro CT image scanning and processing.

Author contributions

T.Y. and R.B. performed most of the experiments. Z.W. and Y.Q. synthesized and characterized the nanoparticles. B.H., G.N., and R.Z. conceived the study and designed the experiments. T.Y., R.B., and Z.W. collected and analyzed the data. J.W. and Y.W. provided suggestions and technical support for the project. T.Y., R.B., and R.Z. wrote the manuscript. B.H., G.N., and R.Z. supervised all experiments and revised the manuscript. All authors read and approved the manuscript.

Competing interests

T.Y., R.B., Z.W., Y.Q., R.Z., B.H., and G.N. are inventors on a filed provisional application for China patent No. 2024115617826 (“A composite butyrate nanoparticle and its synthesis strategy and application”) submitted by Peking University School of Stomatology and the National Center for Nanoscience and Technology that covers the synthesis strategy and potential therapeutic use of BuNP@Shellac for inflammatory bowel disease and osteoporosis treatment. T.Y., R.B., Z.W., Y.Q., R.Z., B.H., and G.N. declare no other competing interests. J.W. and Y.W. declare no competing interests.

Additional information

Supplementary information The online version contains supplementary material available at https://doi.org/10.1038/s41467-024-55263-1.

Correspondence and requests for materials should be addressed to Ruifang Zhao, Guangjun Nie or Bing Han.

Peer review information *Nature Communications* thanks Luigi Gennari and Zhanju Liu for their contribution to the peer review of this work. A peer review file is available.